



저작자표시-비영리-변경금지 2.0 대한민국

이용자는 아래의 조건을 따르는 경우에 한하여 자유롭게

- 이 저작물을 복제, 배포, 전송, 전시, 공연 및 방송할 수 있습니다.

다음과 같은 조건을 따라야 합니다:



저작자표시. 귀하는 원저작자를 표시하여야 합니다.



비영리. 귀하는 이 저작물을 영리 목적으로 이용할 수 없습니다.



변경금지. 귀하는 이 저작물을 개작, 변형 또는 가공할 수 없습니다.

- 귀하는, 이 저작물의 재이용이나 배포의 경우, 이 저작물에 적용된 이용허락조건을 명확하게 나타내어야 합니다.
- 저작권자로부터 별도의 허가를 받으면 이러한 조건들은 적용되지 않습니다.

저작권법에 따른 이용자의 권리는 위의 내용에 의하여 영향을 받지 않습니다.

이것은 [이용허락규약\(Legal Code\)](#)을 이해하기 쉽게 요약한 것입니다.

[Disclaimer](#)

공학석사 학위논문

고분자 전해질형 연료전지의
산소 전달저항에 대한 모델링

Modeling of Oxygen Transport Resistance
in PEM Fuel Cell

2016년 8월

서울대학교 대학원

기계항공공학부 기계전공

이유일

Abstract

Modeling of Oxygen Transport Resistance in PEM Fuel Cell

Yoo-II Lee

Department of Mechanical and Aerospace Engineering
The Graduate School
Seoul National University

A Polymer Electrolyte Membrane (PEM) fuel cell is recognized as one of the promising clean energy sources that can replace internal combustion engine in the upcoming future. Unfortunately, the widespread usage of the fuel cell has not yet reached due to its high cost. Numerous studies have attempted to lower the overall cost of the fuel cell stack by analyzing and improving an individual cell. The studies can be roughly classified into two main streams of research.

1. Improvement in electrical conductivity by reducing the ionic resistance
2. Reduction of oxygen transport resistance

Recently, the latter has received significant attention. Unfortunately, the oxygen transport resistance is a tough parameter to obtain due to the difficulty involved in the measurement of oxygen concentration or a transfer rate. Therefore, the

modeling approach has attracted the scholars' attention.

The aim of this study is to modify an existing quasi-three-dimensional model to analyze the oxygen transport resistance of the PEM fuel cell under various operating conditions. The model considered three difference kinds of transport mechanism: (1) molecular diffusion; (2) Knudsen diffusion; and (3) liquid-phase diffusion through ionomer film. Also, the model adopted a spherical agglomerate catalyst layer structure in order to estimate the oxygen transport phenomenon, more accurately.

The model was validated against two sets of gas diffusion layers (GDLs) by initially comparing the molecular diffusion resistance at the under-saturated condition and secondly, by comparing polarization curves at the fully saturated condition. The developed model was used to discern the effect of GDL structure on the oxygen transport resistance in a range of current density.

In conclusion, the modified model was able to separate and analyze the individual oxygen transport resistance in PEM fuel cell. The model shows the potential of evaluating the component of the cell by providing the results in quantitative values.

**Keywords: PEM fuel cell, Oxygen transport resistance, Gas diffusion layer,
Quasi-three-dimensional model**

Student Number: 2014-21886

Table of Contents

Abstract	i
List of Figures	v
List of Tables	vii
Nomenclatures	viii
Chapter 1. Introduction	1
1.1. Background	1
1.2. Polymer Electrolyte Membrane (PEM) fuel cell.....	3
1.3. Oxygen transport in PEM fuel cell.....	5
1.4. Oxygen transport resistance	8
1.5. Objective	9
Chapter 2. PEM fuel cell model description	10
2.1. Overview	10
2.2. Assumptions	11
2.3. Discretization	11
2.4. Conservation equations	14
2.5. Gas-phase mass transfer	14
2.6. Liquid-phase mass transfer.....	18
2.7. Agglomerate model	20
2.8. Electrochemical model.....	22
2.9. Pressure drop	24
Chapter 3. PEM fuel cell model validation	26
3.1. Overview	26

3.2.	GDL sample descriptions	26
3.3.	Model parameters	30
3.4.	Experimental setup	32
3.5.	Limiting current density	35
3.5.1.	Experimental conditions.....	35
3.5.2.	Theory	36
3.5.3.	Limiting current density	37
3.6.	Polarization curves	40
Chapter 4.	Results and Discussion	42
4.1.	Under-saturated condition	42
4.1.1.	Limiting current density	43
4.1.1.1.	GDL A	43
4.1.1.2.	GDL B	44
4.1.1.3.	Comparison between A and B	45
4.2.	Over-saturated condition	48
4.2.1.	1 A/cm ² vs. 2 A/cm ²	48
4.2.1.1.	GDL A	49
4.2.1.2.	GDL B	50
4.2.1.3.	Comparison	52
4.2.2.	Oxygen transport resistance trends	55
4.2.2.1.	GDL A	55
4.2.2.2.	GDL B	57
4.2.2.3.	Comparison between A and B	58
4.3.	Further discussion	64
Chapter 5.	Conclusion.....	66
Chapter 6.	Bibliography	68

List of Figures

Figure 1. Schematic diagram of a PEM fuel cell adapted from O’Hayre et al.[12].....	4
Figure 2. Schematic description of oxygen transports in a cathode	5
Figure 3. Discretization of a PEM fuel cell model	13
Figure 4. Schematic diagram of anode/cathode control volumes.....	13
Figure 5. Schematic of an agglomerate model	20
Figure 6. A cross-sectional SEM image of GDL A.....	28
Figure 7. A cross-sectional SEM image of GDL B [48].....	28
Figure 8. Pore size distributions of GDL A and GDL B	29
Figure 9. A schematic of the fuel cell station	33
Figure 10. A single PEM unit cell used in model validation experiments	33
Figure 11. The reduction of effective area using gaskets	34
Figure 12. Comparison of molecular diffusion resistance and other resistances between simulation and experiment (GDL A).....	38
Figure 13. Comparison of molecular diffusion resistance and other resistances between simulation and experiment (GDL B).....	39
Figure 14. Comparison of experimental polarization curve and simulated polarization curve (GDL A)	41
Figure 15. Comparison of experimental polarization curve and simulated polarization curve (GDL B)	41
Figure 16. Oxygen transport resistance of each component at under-saturated condition (GDL A).....	44
Figure 17. Oxygen transport resistance of each component at under-saturated condition (GDL B).....	45
Figure 18. Contribution of individual oxygen transport resistance at under-saturated condition (GDL A)	47
Figure 19. Contribution of individual oxygen transport resistance at under-saturated condition (GDL B)	47
Figure 20. Total oxygen transport resistance at 1 A/cm ² and 2 A/cm ² (GDL A)	49

Figure 21. Individual transport resistance at 1 A/cm ² and 2 A/cm ² (GDL A)	50
Figure 22. Total oxygen transport resistance at 1 A/cm ² and 2 A/cm ² (GDL B)	51
Figure 23. Individual transport resistance at 1 A/cm ² and 2 A/cm ² (GDL A)	51
Figure 24. Contribution of individual resistance at 1A/cm ² and 2 A/cm ² for a) GDL A, b) GDL B	53
Figure 25. Water saturation profile at 1 A/cm ² and 2 A/cm ² for a) GDL A b) GDL B	54
Figure 26. Total oxygen transport resistance of GDL A	56
Figure 27. The change in individual oxygen transport resistance between 0.4 A/cm ² to 2.0 A/cm ² (GDL A)	56
Figure 28. Total oxygen transport resistance of GDL B	57
Figure 29. The change in individual oxygen transport resistance between 0.4 A/cm ² to 2.0 A/cm ² (GDL B)	58
Figure 30. Total oxygen transport resistance under various operating current densities.	60
Figure 31. The change in ionomer resistance under various current densities	60
Figure 32. The change in water film resistance and water film thickness under various current densities	61
Figure 33. The change in catalyst layer resistance under various current densities	61
Figure 34. The change in MPL resistance under various current densities	62
Figure 35. The change in substrate resistance under various current densities	62
Figure 36. The change in channel resistance under current densities	63
Figure 37. Comparison of activation overvoltage and Ohmic overvoltage obtained from simulation	63

List of Tables

Table 1. Diffusion volume of simple molecules [31].....	15
Table 2. Laminar friction constants for rectangular channel [47].....	25
Table 3. Estimated physical parameters of GDL and catalyst layer	31
Table 4. Model parameters.....	32
Table 5. Dimension of channels.....	32
Table 6. Experimental condition for limiting current density tests.....	35
Table 7. Limiting current density results	38
Table 8. Experimental condition for polarization curves.....	40

Nomenclatures

C	concentration
D	diffusion coefficient
D_{CF}	carbon fiber diameter
D_h	hydraulic diameter
d_p	pore diameter
F	Faraday constant
<i>f</i>	friction coefficient
<i>g</i>	gravitational force
H	Henry's Law constant
h_m	mass transfer coefficient
K	permeability
K_B	Boltzmann constant
Kn	Knudsen number
M	molar mass
n	number of electrons transferred
N_{agg}	agglomerate density, 1/m ³
R	gas constant
Re	Reynolds number
Ro	estimated solvent radius
s	water saturation
Sh	Sherwood number
<i>x</i>	mole fraction

Greek letters

<i>α</i>	transfer coefficient
<i>δ</i>	thickness
<i>ε</i>	porosity
<i>η</i>	overpotential
<i>κ</i>	conductivity
<i>λ</i>	mean free path
<i>μ</i>	viscosity
<i>v</i>	diffusion volume of molecules

Subscripts and superscripts

act	activation
agg	agglomerate
cl	catalyst layer
eff	effective
g	gas
ion	ionomer
knd	Knudsen
mix	mixture
ohm	ohmic
ref	reference
w	water

Abbreviations

PEM	Polymer Electrolyte Membrane / Proton Exchange Membrane
GDL	Gas Diffusion Layer
PEN	Penetration
MPL	Microporous Layer
CL	Catalyst Layer
MEA	Membrane Electrode Assembly
RH	Relative Humidity
OCV	Open Circuit Voltage
SEM	Scanning Electron Microscope
MFC	Mass Flow Controller
LPM	Liter Per Minute
SR	Stoichiometric Ratio
ICE	Internal Combustion Engine

Chapter 1. Introduction

1.1. Background

During the late 18th and early 19th centuries in Britain, there was a milestone in human history, the Industrial Revolution. The utilization of fossil fuel and the transition from hand production methods to machine manufacture have modernized our way of living beyond imaginations. However, the indiscreet use of fossil fuel and the lack of knowledge on incidental effects on the environment have dramatically polluted the earth's atmosphere and resulted in "global warming".

Fortunately, for the last few decades, a large number of countries have considered the climate change caused by global warming as a single biggest environmental and humanitarian issue of our time. Since transportation is regarded as one of the main sources of air pollution (including greenhouse gas emission), legislations and regulations on automotive vehicle emissions have been established and continuously enhancing to restrain and minimize the environmental damage [1]. Accordingly, automotive manufacturers have been developing and improving the combustion engine technologies to satisfy the current fuel and emission standards and other enhanced standards to come. However, as relevant regulations become increasingly stringent, it seems difficult to meet the fuel and emission standards solely with a conventional combustion engine. This prediction has been supported by the series of emission-cheating and fuel mileage scandal from major automakers [2, 3]. As a result, alternative ways of powering vehicles have devised in both entrepreneur's and customer's minds.

One of the promising replacement for internal combustion engine (ICE) is a fuel cell. Unlike an ICE, which produces harmful exhaust gas, a polymer electrolyte membrane (PEM) fuel cell operates at a low temperature ($\sim 80^{\circ}\text{C}$) and produce water and heat only. Moreover, provided that the hydrogen is produced using renewable energy, it is a self-sustainable energy source without any damage to the environment. Besides the eco-friendly aspect, fuel cells have a few advantages over ICEs. Firstly, fuel cells directly generate electricity through an electrochemical reaction; hence they do not require any moving components and offers opportunities to make the system more reliable and quiet. Additionally, they avoid Carnot limitation and achieves much higher efficiency. However, the commercialization of fuel-cell powered vehicles has been delayed due to its durability and expensiveness concerns [4].

Consequently, the comprehensive researches have been carried out to improve the overall output of a cell while ensuring both mechanical and chemical durability of an individual fuel cell component, for instance, a gas diffusion layer (GDL), a microporous layer (MPL) and so on [5-9]. Furthermore, substantial efforts have been made to lower the price of the stack to the ICE level by developing non-precious metal catalysts to replace the expensive platinum catalysts [10, 11]. As the result of these continuous studies, a significant improvement on PEM fuel cells have been made, and the commercialization of fuel cells now is one step closer.

1.2. Polymer Electrolyte Membrane (PEM) fuel cell

A PEM fuel cell is a type of fuel cell that utilizes a polymer membrane as an electrolyte. The main advantage of this kind of fuel cell is the ability to operate at a relatively low temperature ($\sim 80^{\circ}\text{C}$) with high power density. Therefore, a PEM fuel cell has been recognized as a choice for an alternative portable power source including the automotive application.

The fundamental principle of fuel cells is straightforward. It is the reverse reaction of water electrolysis as listed on the following equation.



To harness the electrical energy from this reaction, polymer electrolyte membranes are used. The noticeable feature of these membranes is the ability to allow the movement of protons while blocking electrons. The division of protons and electrons paths allows an external load circuit to be created. As shown in Figure 1, hydrogen oxidation occurs at the anode, and hydrogen ions and electrons travel through their individual path to react with oxygen at the cathode. Hence, the movement of the electron grants the utilization of electrical energy generated from the electrochemical reaction.

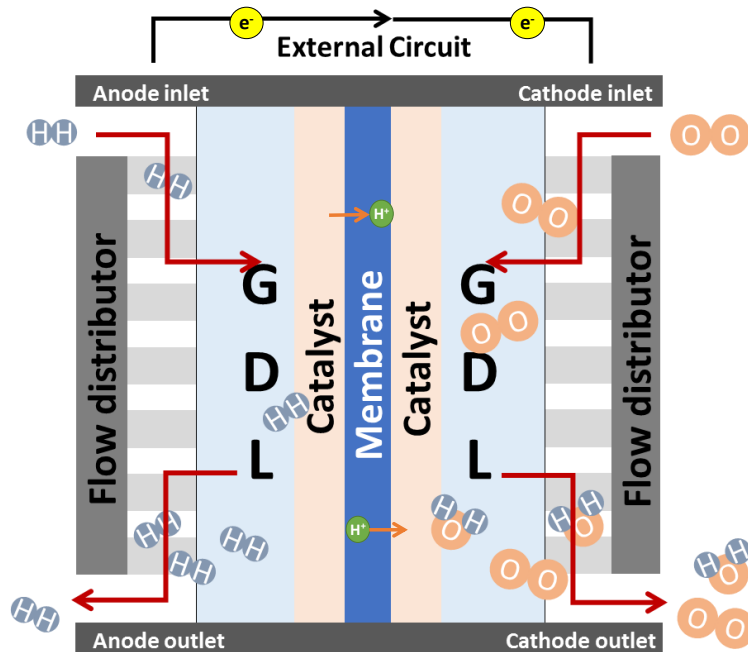


Figure 1. Schematic diagram of a PEM fuel cell adapted from O’Hayre et al.[12]

The voltage output of the cell is sensitively affected by the catalyst condition. According to the Nernst equation and Butler-Volmer equation, the concentration of reactant gas at the catalyst surface severely influences the cell performance; hence, to achieve high reactant concentration, the cell should possess the ability to transport the reactant gas effectively, as well as to efficiently remove any excessive liquid water. The most of the focus on the reactant transport is limited to the cathode due to the following reasons. Firstly, the water is produced at the cathode catalyst. Secondly, the reactant fuel for the cathode is usually the air that only consists of 21% of oxygen. Lastly, the rate of oxygen reduction reaction is much slower than that of the hydrogen oxidation reaction. Therefore, numerous studies have been conducted to improve the cell performance by focusing on oxygen transport phenomenon.

1.3. Oxygen transport in PEM fuel cell

The oxygen transport from the cathode flow-field to the platinum surface in the catalyst layer is conceptualized as shown in Figure 2. The transport of the oxygen molecules can be divided into the following components:

- 1) Flow-field region.
- 2) GDL with MPL region.
- 3) Catalyst layer region.

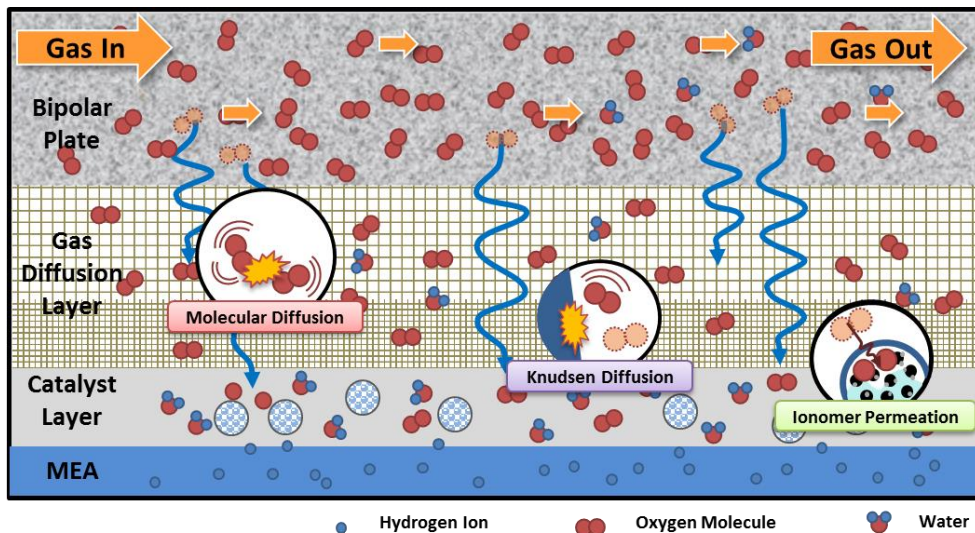


Figure 2. Schematic description of oxygen transports in a cathode

Due to the difference in physical properties, the primary oxygen transport mechanism for each layer might vary. At the flow-fields, a reactant gas is subjected to convective force and transported along the channel at a rapid rate. As the gas enters the substrate in GDL, the mode of transport changes from convection to diffusion. The average pore diameter of the substrate is much larger than the mean free path of

gas molecules. Consequently, the interaction between gas molecules becomes the main driving force of diffusion, that is, molecular diffusion. As oxygen passes through the substrate of GDL, it encounters much smaller pores at the MPL of GDL and the catalyst layer. As the pore diameter approximates to the figure of mean free path of the gas molecules, the molecules start to collide frequently with the diffusion medium. The diffusion process, caused by the collision of molecules and the medium, is called Knudsen diffusion. As a result, the diffusion at the MPL and the catalyst layer is no longer solely molecular diffusion, but the combination of molecular and Knudsen diffusion. After reaching the catalyst agglomerate, oxygen has to be dissolved to permeate the ionomer covering the agglomerate. These are the oxygen transport mechanisms and a brief idea of oxygen transport resistance for each component.

In recent years, numerous researches on fuel cell components such as GDLs, catalysts, and bipolar plates, have been conducted to reduce the oxygen transport resistance and increase the operating power range of the cell [13-18]. One of the attempts to minimize the oxygen transport resistance focuses on the flow-field. A conventional flow-field is a graphite plate carved in channels. The reduction of the rib area decreases the transport resistance at the channel-GDL interface and attributes to a higher distribution of reactant gas. Therefore, it was reported that minimizing the widths of the channels and the ribs increases a cell performance [19].

Kumar and Reddy [18] had replaced the channel-inscribed flow-field with metal foam to remove the existence of ribs. Similar research regarding the porous flow distributor was attempted [20]. Despite the positive effect on the interfacial area between channels and GDLs, the adoption of porous medium presents new problems.

Firstly, the introduction of the foam structure significantly increases the pressure drop, in other words, it requires a higher power compressor that increases the auxiliary power consumption. Secondly, even with the higher compressor, a substantial amount of residual water tends to stay in pores, reducing both stack performance and stability. By combining the benefits of the conventional flow-field and porous flow-field, a three-dimensional fine-mesh flow-field was developed by Toyota Motors [21]. The developed flow-field separated the airway and waterway for the purpose of promoting oxygen diffusion at the catalyst layer and expelling the generated water to the outer surface of the 3D fine mesh flow.

Meanwhile, some have employed a variation in GDL property in the through-plane direction to endorse the removal of excess liquid water at high humidity conditions, and at the same time, maintain higher membrane water contents at low humidity conditions [13]. Others have removed GDLs to improve the cell performance as the porous field could compensate their absence [22].

1.4. Oxygen transport resistance

The reduction in oxygen transport resistances is the key to a higher cell performance. Hence, there have been studies concerned specifically with the measurement of oxygen transport resistance in each component. Beuscher [23] suggested a simple mean of measuring mass transport resistance using limiting current densities. By changing carrier gases and the number of GDLs, the author found that the GDL was responsible for about 25% of the total transport resistance. In addition, the analysis reveals that the resistance from Knudsen diffusion, ionomer permeation, and water film accounted 56% of the total resistance. Baker et al. [24] also separated the oxygen transport resistance into the channel, substrate, MPL and other resistance. The authors conducted the experiments at the condition when the cell was adequately humidified, but no liquid water condensed. In this study, the contributions of the diffusion medium, channel, microporous layer, and others were 53%, 24%, 8% and 15%, respectively. In 2011, Nonoyama et al. [25] divided the total oxygen transport resistance into the molecular, Knudsen and ionomer film resistance by varying operating temperature and balance gas. The authors concluded that the ionomer resistance took significant portions of transport resistance at low temperature and humidity conditions.

An experimental approach to the measurement of oxygen transport resistance of individual layer requires a series of experiments. In addition, due to the difficulty associated with the liquid water effect, the majority of the published experiments were limited to under-saturated conditions. Therefore, to overcome these obstacles, a computer modeling approach is recommended as one of the solutions.

1.5. Objective

The main purpose of the study is to modify an existing quasi-three-dimensional model to estimate the oxygen transport resistance by each component under various operating conditions.

To properly predict the oxygen transport resistance, substantial revisions were made on the model created and modified by Kang [26] and Park [27]. Originally, the PEM fuel cell model was developed as a part of the integrated PEM fuel cell electrical vehicle system. As a result, the transport phenomena was simplified using binary diffusion coefficients and thin catalyst layer models. To adequately capture the real transport phenomenon, the model had undergone major revisions on the oxygen transport mechanism to consider multicomponent mixture, Knudsen diffusion, and agglomerate catalyst model. The developed model was firstly validated against the experimental results by comparing the limiting current density results of two-percent oxygen with nitrogen and one with helium diluent. This validation confirmed the ability of the developed model to estimate the total oxygen transport resistance and the contribution of molecular diffusion resistance from the total. Secondly, the current-voltage curves results were juxtaposed to verify its capability to imitate the transport phenomena on normal operating conditions.

In this study, the current density was varied to examine the effect of the operating point on the transport resistance. Moreover, two different sets of GDLs with distinct physical properties namely, GDL A and GDL B were analyzed to observe the effect of the GDL on the individual oxygen transport resistance.

Chapter 2. PEM fuel cell model description

2.1. Overview

The model used in this study was a quasi-three-dimensional dynamic model based on MATLAB®/Simulink® platform. A one-dimensional PEM fuel cell node was created in through-plane direction, then it was reproduced to be arranged in an in-plane direction to form a quasi-three-dimensional model. This approach allowed the model to modestly reflect the spatial characteristics of the cell along the channel with lesser computation power, compared to the full-scale three-dimensional model [27].

Several changes to the previous model were made to accurately compute the oxygen transport resistance during various cell operation conditions. The introduction to the previous model are as follows:

- 1) Multicomponent diffusion
- 2) Knudsen diffusion, and
- 3) Agglomerate catalyst layer model

In addition, the control of inlet oxygen concentration and the selection of the inert gas were supplemented to provide the mean of comparing acquired simulation results against empirical results.

2.2. Assumptions

A number of assumptions were employed to decrease the computational time without significantly degrading the accuracy of the result. In addition to the major assumptions adopted by Kang [26], the following assumptions were made to reflect the agglomerate structure.

1. Liquid water in the catalyst covers the agglomerates and create a water coating layer [28].
2. The agglomerates are located near catalyst-MEA interface.
3. The transport inside the agglomerates is ignored.

2.3. Discretization

A PEM fuel cell model was discretized to into several control volumes to sufficiently describe the behavior of a cell. Firstly, the fuel cell was discretized in a direction perpendicular to the gas stream, and then in the flow direction to capture and imitate the mass transport phenomena such as convection, diffusion, and capillary water flux (Figure 3). A PEM fuel cell is consisted of bipolar plates with channels, GDLs with MPL, and a membrane-electrode-assembly (MEA). The minimum of one control volume was allotted to apprehend the mass and heat transfer for each component. In the previous studies, the temperature of the cell was manipulated by the coolant flowing through the flow channels. However, in this study, the temperature of the cell was regulated by heating poles, plunged into the holes in bipolar plates. Hence, the needs for coolant channels and coolant plates were unnecessary. Therefore, those were suppressed to reduce the computation time. MPLs are in contact with MEA and

have a pore size around hundred nanometers while substrates have near hundred micrometers. Accordingly, the mass transport phenomenon such as oxygen diffusion and capillary flux is highly affected by its location on GDL. As a result, the control volumes of eight were selected for each GDL to replicate the variation of the physical properties as shown in Figure 4. Noticeable, five control volumes were assigned to the substrate while the MPL were assigned with three. The discretization along the flow direction influences the cell performance by reflecting the change in gas compositions due to fuel depletion and water generation. It was intimated that the detail discretization of the cell would increase the accuracy of the model. However, it would significantly put a strain on the PEM model and demand a higher computing power. Since the model was originally developed for the control and system design tools [29], the maximum discretization number of 35 was limited to ensure the fast calculation speed and the model compactness.

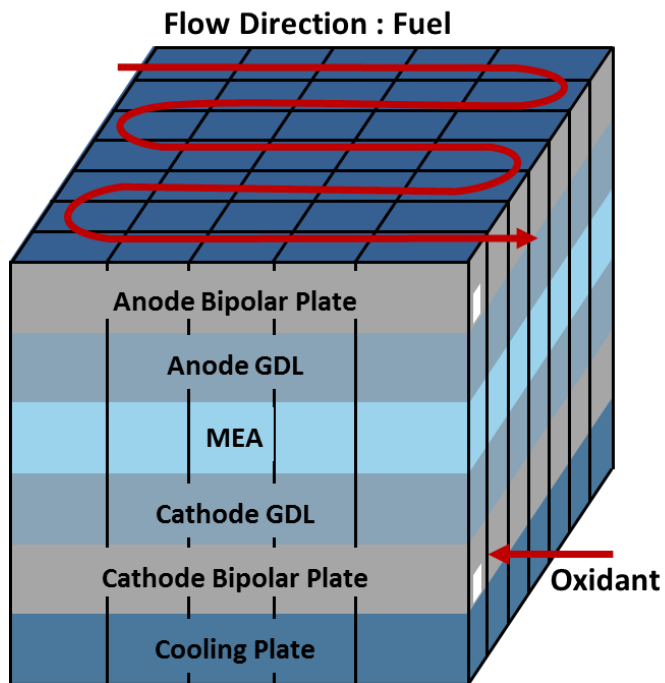


Figure 3. Discretization of a PEM fuel cell model

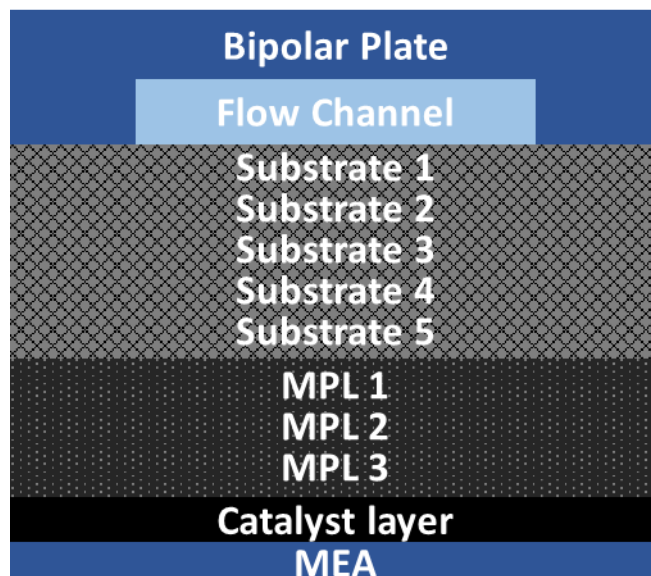


Figure 4. Schematic diagram of anode/cathode control volumes

2.4. Conservation equations

For each control volume, conservation of energy and conservation of species were employed to determine the local temperatures, mole fractions, and their flux. Specifically, Newton's law of cooling and Fourier's law were used to obtain the heat rate. The "perfect mixing" assumptions were made for all control volume in the calculation of molar flux. More detailed descriptions of conservation equations can be found in Reference [26].

2.5. Gas-phase mass transfer

All the reactants of the PEM fuel cell were supplied in gaseous form. Consequently, the comprehensive modeling of gas-phase mass transfer was a critical factor in accurately estimating the oxygen transport resistance. The previous model utilized binary diffusion coefficient constants and used the saturation of control volume to modify the diffusion coefficients. Even though it was able to imitate the effects of saturation,

it could not reflect the change in diffusion coefficient due to the change in gas composition. In addition, preceding model ignored Knudsen diffusion and ionomer resistance. For these reasons, new equations were introduced to estimate the effective diffusion coefficient of each control volume using proper diffusion mechanism. In the following subsections, the method of selecting appropriate oxygen transport mechanism and calculating effective coefficient will be elaborated.

2.5.1 Diffusion Coefficient

The diffusion coefficient of gas is affected by a number of factors such as a temperature, pressure, composition and property of the diffusion medium. The molecular diffusion coefficient was calculated using both the binary diffusion equation and the multicomponent mixture gas equation for each control volume. For MPLs and catalyst layers, the effective diffusion coefficients were computed by harmonic averaging of molecular diffusion and Knudsen diffusion.

Firstly, the binary gas diffusion coefficient was predicted using the equation developed by Fuller et al. [30].

$$D_{AB}(cm^2/s) = \frac{1.00 \times 10^{-3} T^{1.75} \left(\frac{1}{M_A} + \frac{1}{M_B} \right)^{0.5}}{P \left[(\sum v_A)^{\frac{1}{3}} + (\sum v_B)^{\frac{1}{3}} \right]^2} \quad (2.1)$$

The unit for temperatures and pressures are in Kelvin and atmosphere, respectively.

M is the molar mass of the molecule.

v is the diffusion volume of molecules.

Table 1. Diffusion volume of simple molecules [31]

Species	Diffusion Volume	Species	Diffusion Volume
Nitrogen	17.9	Water	12.7
Helium	2.88	Hydrogen	7.07
Oxygen	16.6		

Secondly, a multicomponent equation was used to acknowledge the effect of the gas composition. In a cathode side, nitrogen, oxygen, and water vapor gas exist, making a tertiary gas composition. Thus, the molecular diffusion coefficient in mixture gas was estimated by the relation verified by Fairbanks and Wilke [32].

$$D_{A-mix} = \frac{1-y_A}{\frac{y_B}{D_{AB}} + \frac{y_C}{D_{AC}} + \frac{y_D}{D_{AD}} + \dots} \quad (2.2)$$

Thirdly, Knudsen number was used as a criterion to determine the appropriate diffusion mechanism for each control volume.

$$k_n = \frac{\lambda}{d_p} \begin{cases} k_n < 0.01 & \text{Molecular region} \\ 0.01 \leq k_n \leq 10 & \text{Transition region} \\ k_n > 10 & \text{Knudsen region} \end{cases} \quad (2.3)$$

In the calculation of Knudsen number, mean free path in mixture gas was used [33].

$$\lambda_i = \frac{1}{\sum_{j=1}^N \pi (r_i + r_j)^2 n_j \sqrt{1 + \left(\frac{m_i}{m_j}\right)}} \quad (2.4)$$

Then, to calculate the diffusion coefficient for transition or Knudsen region, the following equation was used to derive the Knudsen diffusion coefficient [34].

$$D_{i-knud} = \frac{d_p}{3} \sqrt{\frac{8RT}{\pi M_i}} \quad (2.5)$$

During the transition region, both diffusion mechanism should be considered. Thus, Bosanquet formula was used to include both contribution as below [35].

$$D_{combined} = \left(\frac{1}{D_{i-mix}} + \frac{1}{D_{i-knud}} \right)^{-1} \text{ (for } 0.01 \leq K_n \leq 10) \quad (2.6)$$

2.5.2 Gas-phase mass transfer in GDL

For convective mass transfer between the gas channel and GDL, the following equations were used [36].

$$\vec{\Phi}_{conv} = \vec{h}_m A (C_{i,channel} - C_{i,GDL}) \quad (2.7)$$

$$\vec{h}_m = \frac{Sh \cdot \bar{D}_m}{D_h} \quad (2.8)$$

For diffusion mass transfer, the diffusion length of the porous material is affected by the tortuosity of the material. The estimation of the tortuosity is challenging due to the randomness of the carbon fiber stacks; hence, Bruggeman correlation was used to estimate the effect of the tortuosity [37].

$$\bar{D}_m^{eff} = [\varepsilon(1 - s)]^{1.5} \bar{D}_m^g \quad (2.9)$$

Diffusion mass transfer rate was modeled based on Darcy's equation as the following equation.

$$\vec{\Phi}_{diff} = \frac{\bar{D}_m^{eff} A}{t} (C_{i+1} - C_i) \quad (2.10)$$

2.6. Liquid-phase mass transfer

The management of the liquid water in PEM fuel cells are vital in achieving high performance. The formation of liquid water blocks the pores in the catalyst layer and covers the agglomerate with water films. Consequently, the oxygen transfer rate decreases and cell voltage deteriorates. On the contrary, the presence of liquid water at membrane causes a sharp change in water uptake, as known as Schroeder's paradox, and helps to lower the membrane conductivity [37]. Therefore, the control of liquid water is essential in determining accurate cell voltage; hence the liquid water transfer was prudently modeled using the multiphase mixture formation, developed by Wang et al. [38].

In this model, most of the equation relating to the liquid-phase mass transfer is the same as previous Kang's model [26]. However, few modifications were made to improve the prediction of the liquid water flux.

Firstly, the relative permeability model was changed as it was reported that the following relation is more appropriate for diffusion medium [39].

$$k_{rl} = s^{2.16}, k_{rg} = (1 - s)^{2.16} \quad (2.11)$$

Secondly, the method of estimating the permeability was replaced. The permeability is often calculated using the Kozeny-Carman relation [40] using pore diameter and porosity. However, it is not suitable for fibrous materials such as GDLs, and it cannot accurately calculate the permeability in the transition flow regimes. Therefore, the

permeability of the fibrous porous media was calculated using the equation formulated by Jeong et al. [41].

$$\frac{K}{D_{CF}^2} = \exp \left\{ C_1 \ln \left(\frac{\frac{11}{\varepsilon^3}}{(1-\varepsilon)^2} \right) - C_2 \right\} \quad (2.12)$$

$$\begin{cases} C_1 = 0.7128 - 0.4953K_n \\ C_2 = 1.974 - 4.2892 \end{cases}$$

Thirdly, the water diffusion coefficient was halved. The equation used to calculate the water diffusion coefficient in the membrane was for Nafion™ membrane. However, the membranes from Gore company were used in this study. Therefore, the previous equation was not directly applicable. In 2007, Ye and Yang [42] experimentally measured the water diffusion coefficient of Gore-Select membrane and found that it was roughly the half of Nafion membrane. Therefore, in this study, the membrane was assumed to be consisted of 50% of Nafion materials.

$$D_{w,eff} = 0.5D_w \quad (2.13)$$

2.7. Agglomerate model

The preceding model assumed that the catalyst layer is thin, and the structure of its layer could be ignored. However, experimental results revealed that the oxygen transport resistance in a catalyst layer contributes to the 15% of the total dry transport resistance [24]. Therefore, the porous electrode model was introduced to reflect the agglomerate structure in oxygen transport phenomena while assuming uniform concentration and potential across the layer [36]. As shown in Figure 5, it is modeled that the ionomer film entirely covers the agglomerate surface. Additionally, any residing liquid water in the catalyst layer was assumed to form water films around ionomers as shown in the equation below [28].

$$\delta_w = \sqrt[3]{(r_{agg} + \delta_{ion})^3 + \frac{3S\epsilon_{cl}}{4\pi N_{agg}}} - (r_{agg} + \delta_{ion}) \quad (2.14)$$

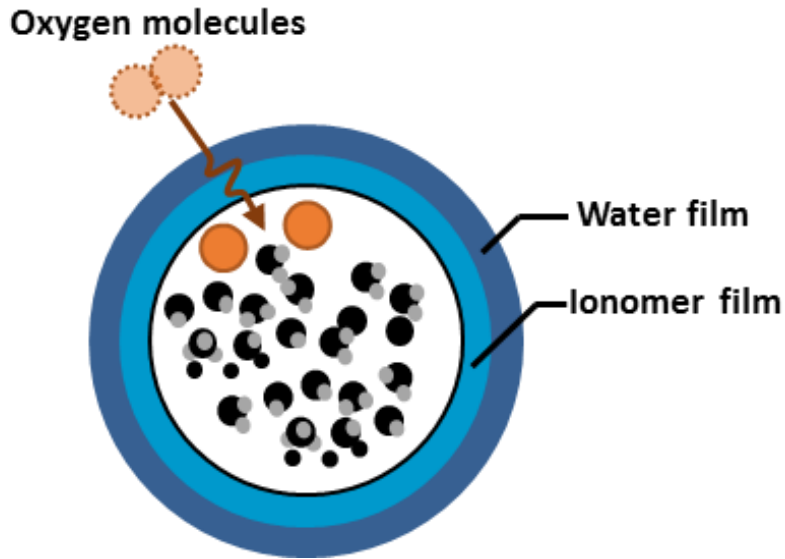


Figure 5. Schematic of an agglomerate model

To reach the reaction site, oxygen molecules have to be dissolved and transported through one or two layers. Since the oxygen molecules are transported across a phase boundary, the discontinuous molar concentration occurs at the phase interface. The concentration discontinuity was modeled with Henry's constants obtained by experimental results [28]:

$$H_{O_2}(Pa \cdot m^3 \cdot mol^{-1}) = 0.11552 \exp\left(14.1 + 0.0302\lambda - \frac{666}{T}\right) \quad (2.15)$$

The liquid-phase diffusion of oxygen molecules was estimated using the Stokes-Einstein equation:

$$D_{O_2-H_2O} = \frac{k_B T}{6\pi\mu R_o} \quad (2.16)$$

R_o is the estimated solvent radius, and the value for oxygen is 1.734 ångström.

The oxygen diffusivity in Nafion® ionomer was corrected by Marr and Li [43] as

$$D_{O_2-M}^{eff} = 1.3926 \times 10^{-10} \lambda^{0.708} \exp\left(\frac{T - 273.15}{106.65}\right) - 1.6461 \times 10^{-10} \lambda^{0.708} + 5.2 \times 10^{-10} \quad (2.17)$$

2.8. Electrochemical model

The nodal voltage was calculated by subtracting the activation overvoltage and ohmic overvoltage from the open circuit voltage.

$$V_{cell} = V_{OCV} - \eta_{act} - \eta_{ohm} \quad (2.18)$$

The previous model used the theoretical reversible voltage as a constant term of Nernst equation. However, the theoretical reversible voltage tends to over-predict the open circuit voltage, as it does not consider the effects of voltage drop due to the fuel crossover and the mixed potential of the Pt/PtO catalyst surface [44].

Therefore, the calculation of the open circuit voltage was correlated by Eq. (2.19) [45] and the Nernst equation.

$$V_{OC+} = 0.0025T + 0.2329 \quad (2.19)$$

$$V_{OCV} = V_{oc+} + \frac{\Delta\hat{s}}{nF}(T - T_0) - \frac{RT}{nF} \ln \frac{\prod a_{products}^{v_i}}{\prod a_{reactants}^{v_i}} \quad (2.20)$$

For activation overvoltage, only the cathodic reaction kinetics was considered, and the simplified form of Butler-Volmer equation was used. Due to the introduction of the water film, the saturation effects were removed from the previous model to avoid redundancy.

$$\eta_{act} = \frac{RT}{\alpha F} \ln \left(\frac{j}{j_o} \frac{C_{O_2}^{ref}}{C_{O_2}} \right) \quad (2.21)$$

The ionic conductivity of Nafion is dependent on water content as shown in Eq. (2.22) [12]. The proton conductivity of the membrane was assumed to be the half of the Nafion membrane.

$$\kappa = (0.005139\lambda - 0.00326) \exp\left(1268\left(\frac{1}{303} - \frac{1}{T}\right)\right) \quad (2.22)$$

$$\kappa_{eff} = 0.5\kappa \quad (2.23)$$

Then, the sum of the resistance was expressed by the following equation.

$$R_{ohm} = \frac{t_{mea}}{\kappa_{eff}} + \frac{2t_{GDL}}{\sigma} + R_{contact} \quad (2.24)$$

Using the Ohm's law, the ohmic overvoltage was obtained.

$$\eta_{ohm} = IR_{ohm} \quad (2.25)$$

Due to the equipotential electrode assumption, entire nodes of the cell had to be the identical value. Thus, the nodal current was iterated until all the cell voltage was equal, satisfying the following equation.

$$V_{cell} = V_{node} = \sum I_{node}R \quad (2.26)$$

2.9. Pressure drop

The gas pressure in the PEM fuel cell varies node by node due to the following reasons. Firstly, the electrochemical reaction alters the number of the molecules in each channel. Secondly, the supplied gas experiences a frictional force as it travels through the flow channel. The former is negligible and not reflected in the model. However, pressure drop due to the frictional shear force could not be overlooked. Therefore, the calculation of Reynolds number and the friction coefficient were calculated using Eq. (2.27) to Eq. (2.28). For friction coefficients for the turbulent flow, Filonenko equation was used, presuming the smooth surface [46].

1. Laminar Flow:

$$Re = \frac{\rho v D_H}{\mu} \quad (2.27)$$

$$Re < 2300, f = \frac{fRe}{Re} \quad (2.28)$$

2. Turbulent Flow

$$Re \geq 2300, D_{eff} = \left[\frac{64}{fRe} \right] D_H \quad (2.29)$$

$$Re_{eff} = \frac{\rho v D_{eff}}{\mu} \quad (2.30)$$

$$f = (1.82 \log_{10} Re - 1.64)^{-2} \quad (2.31)$$

Table 2. Laminar friction constants for rectangular channel [47]

height / width	fRe	height / width	fRe
0.0	96.00	0.25	72.93
0.05	89.91	0.4	65.47
0.1	84.68	0.5	62.19
0.125	82.34	0.75	57.89
0.167	78.81	1.0	56.91

In addition to the major head loss, minor head losses were introduced in this model to capture the effect of the pressure drop around the sharp corners. Through Eq. (2.32) to Eq. (2.35), the major and minor head losses were calculated, and the pressure drop for each node was computed.

$$h_f = f \frac{L}{D_h} \frac{v^2}{2g} \quad (2.32)$$

$$h_m = \frac{v^2}{2g} \Sigma K \quad (2.33)$$

$$h_{total} = h_f + h_m \quad (2.34)$$

$$\Delta p = \rho g h_{total} \quad (2.35)$$

Chapter 3. PEM fuel cell model validation

3.1. Overview

Model validation was conducted by comparing the limiting current result and current-voltage curve. Firstly, the limiting current density of the cells was obtained both empirically and theoretically by using two-percent oxygen with nitrogen and helium diluent. The comparison of limiting current density results verified the model's ability to analyze the molecular diffusion resistance from other resistance at under-saturated water vapor condition. Secondly, the model was simulated to draw a polarization curve at fully humidified condition. The polarization curves of both simulation and experimental results were compared to confirm the proper estimation of oxygen transport resistance at over-saturated condition.

3.2. GDL sample descriptions

In this study, two sets of GDLs with distinct physical properties were selected to observe the oxygen transport resistance of the individual component. Both GDL samples were the carbon paper-type GDL with an MPL coating. They were manufactured by different companies and will be referred as "A" and "B". Due to the number of the speculations made on the physical properties, the sample name, as well as the name of the company were undisclosed.

Scanning electron microscope (SEM) images clearly revealed a noticeable difference between those two GDLs (Figures 6 and 7). Carbon fibers in GDL A were straight and appeared rigid. By contrast, fibers in GDL looked more flexible. As suspected from the SEM image, GDL A was more brittle than GDL B, making it more vulnerable to the impact. In addition, GDL A seemed to have a larger void volume in substrate (Figure 6). Another noticeable difference was the appearances of the MPL. The images indicated that MPLs of both GDLs are undoubtedly dissimilar which may lead to the change in oxygen transport resistance. Moreover, GDL B showed a clear borderline between MPL and substrate. In opposition to this, MPL of the GDL A sample penetrated deeply into the substrate area, blurring the MPL and substrate borderline as observed in Figure 6.

The pore size distributions of both GDLs were obtained using a mercury porosimetry. Two distinct peaks were seen in the entire pore size range: one peak around 70 nanometers, and the other around 50 micrometers (Figure 8). The smaller pore size peaks were generated by MPL, and it can be characterized as the representative MPL pore size. In a similar fashion, the larger size peaks were produced by carbon fibers in substrates. The results indicated that the pore sizes of MPL and substrate for GDL A and GDL B were 56.3 nm, 70.1 nm, 40.5 μm and 60.5 μm , respectively. At the same time, porosimetry informed that the porosity of the GDL A was 5.71% higher than that of GDL B. It appeared that GDL A was specifically designed to possess the smaller pore size yet exhibit higher porosity.

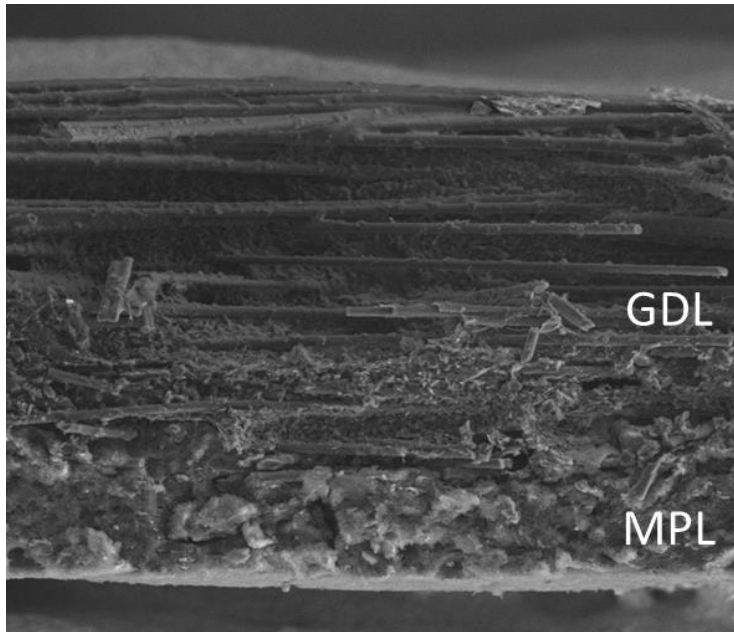


Figure 6. A cross-sectional SEM image of GDL A

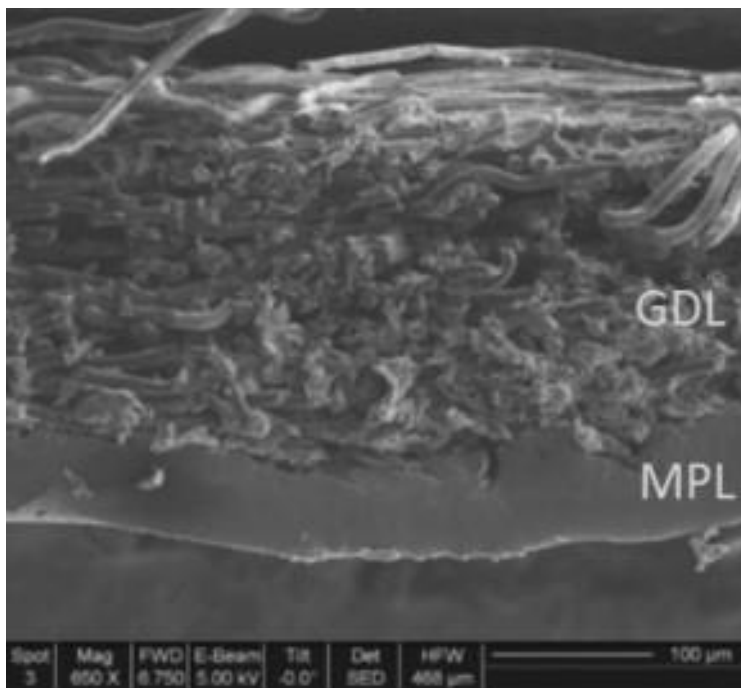


Figure 7. A cross-sectional SEM image of GDL B [48]

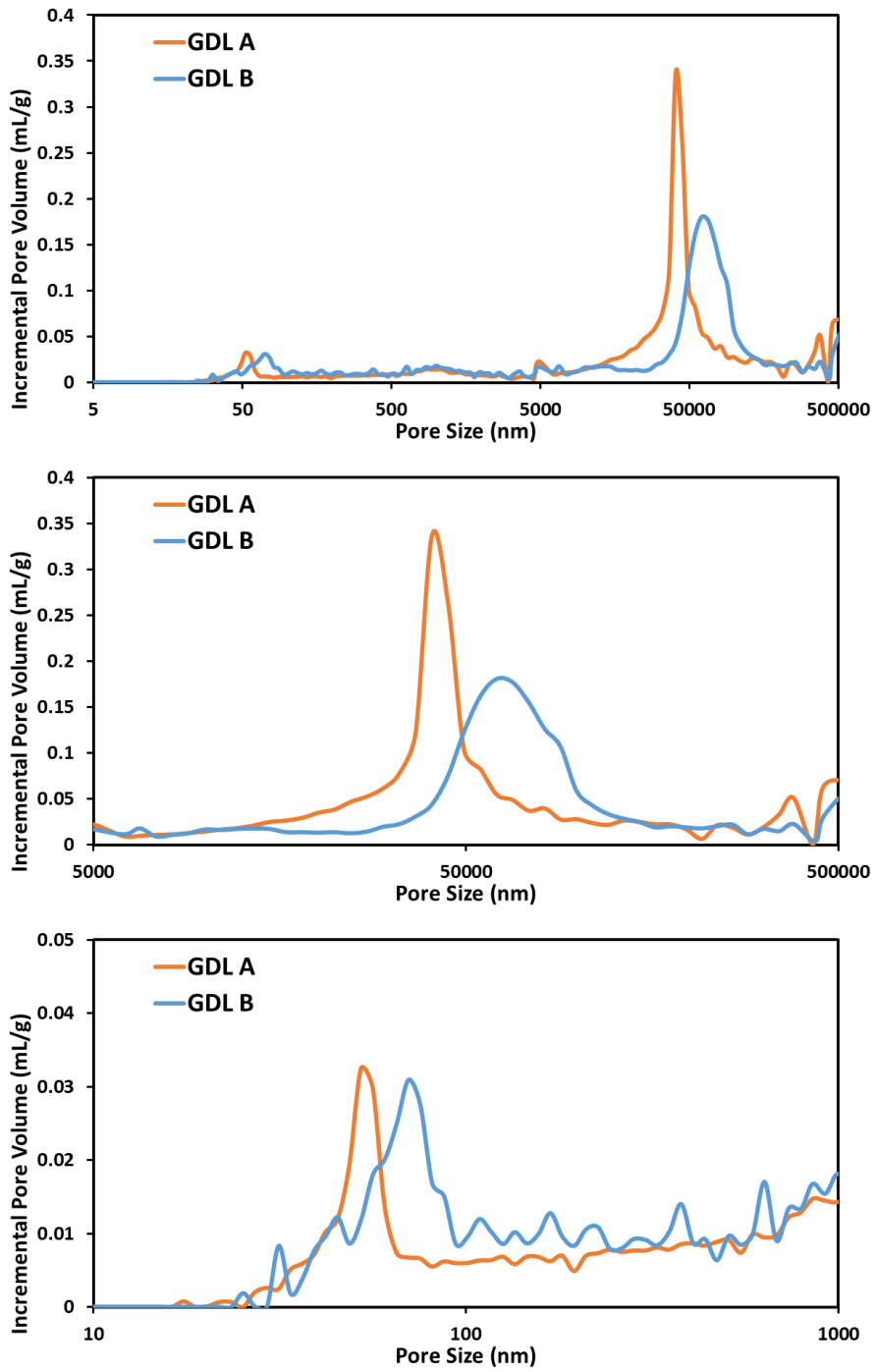


Figure 8. Pore size distributions of GDL A and GDL B

3.3. Model parameters

The model parameters were carefully chosen to mimic the behavior of the fuel cell operation. GDLs are subjected to compressive forces during the cell assembly process and the physical properties such as porosity, thickness and pore size distribution changes. Therefore, the properties such as porosity, thickness, and pore size were measured at pristine conditions and then the severity of the compression effect on each property was judged, and the model inputs were chosen cautiously.

The total GDL thickness was measured with micrometers, and the thickness of the MPL was estimated from the SEM image. The substrate part was assumed to be the only compressible materials due to the high porosity, and compressed substrate thickness was estimated. The measurement on the local porosity is challenging as MPL cannot stand alone. In 2010, Ostadi et al. [49] attained local MPL porosity of 40% using FIB/SEM nano-tomographic 3D reconstruction. In this study, the local porosities were reasonably speculated using the overall GDL porosity results from mercury porosimetry and the MPL porosity of 40%. The average pore size of MPL and substrates were chosen to be the peak values in the pore size distribution data without taking into account the decrease in pore size during the cell assembly. The internal contact angle of GDLs controls the capillary water flux. Therefore, the accurate value for contact angle is critical in simulating water saturation effect.

Due to the difficulty involve in the measurement of agglomerate properties, the values were estimated from the work of others. Firstly, the ionomer film was reported to have a thickness between 3 to 10 nm [50]. Therefore, the ionomer thickness was

selected to be the value of 7 nanometers as stated by Lopez-Haro et al. [51]. The typical agglomerate size is known to be in the range of 50-100 nm [52]. For the agglomerate radius, 87.5 nm was chosen, considering the selected ionomer film thickness.

The catalyst layer was estimated by measuring the total MEA thickness and subtracting ionomer thickness which was provided by the manufacturer. Two peaks were observed in the BET measurement, and they were believed to be responsible for the inter-agglomerate pore size and the intra-agglomerate pore size. However, the intra-agglomerate structure was not considered in this study; hence the average mean pore size of 48.7 nm was used.

Table 3. Estimated physical parameters of GDL and catalyst layer

Description	GDL A	GDL B
Thickness (μm)		
Substrates	214	227
MPLs	30	45
Catalyst Layer	7	
Porosity (%)		
Substrates	85	74
MPLs	40	
Catalyst Layer	36	
Pore size (nm)		
Substrates	40,500	60,500
MPLs	56.3	70.1
Catalyst Layer	48.7	
Internal Contact Angle (degrees)		
Substrates	122.5	118 [48]
MPLs	140.5	99 [48]

Table 4. Model parameters

Parameter	Value	Ref.
Transfer Coefficient	0.567	[53]
Exchange Current Density	4.956e-5 A/cm ²	[43]
No of agglomerate	1.01e19 m ⁻³	Est.
Agglomerate Radius	87.5 nm	Est.
Ionomer film thickness	7 nm	[51]

3.4. Experimental setup

A fuel cell station used in this study is as shown in Figure 9. It was equipped with five individual mass flow controllers (MFCs) to manipulate the composition of inlet gas. For the humidification of the reactant gas, membrane humidifiers were used. Cells were tested with Kikusui electronic load (PLZ664WA), and the corresponding voltage outputs were measured with National Instrument data acquisition board (USB6009) for faster sampling and more accurate measurement. The high-purity gases with over 99.995% purity were used in the experiments. For air, multiple filters and a pneumatic dryer were utilized to remove unwanted particles and moist before entering the station. 25cm² unit cells with quadruple serpentine channels were used in the study. The dimensions of the channels are presented in Table 5. For the limiting current density tests, the effective area was decreased to 1cm² by covering the rest of the effective area with the gasket as shown in Figure 11.

Table 5. Dimension of channels

	Channel Width	Channel Depth
Anode	1 mm	0.4 mm
Cathode	1 mm	0.5 mm

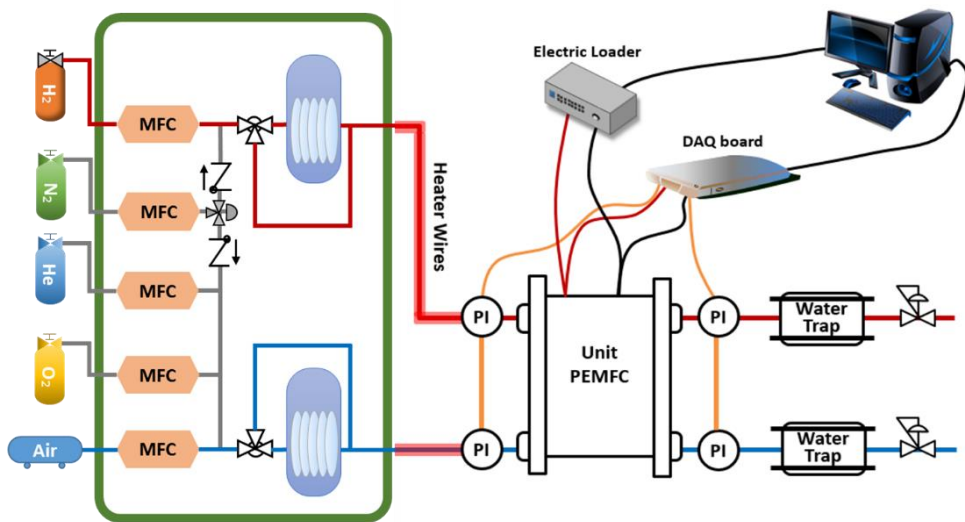


Figure 9. A schematic of the fuel cell station

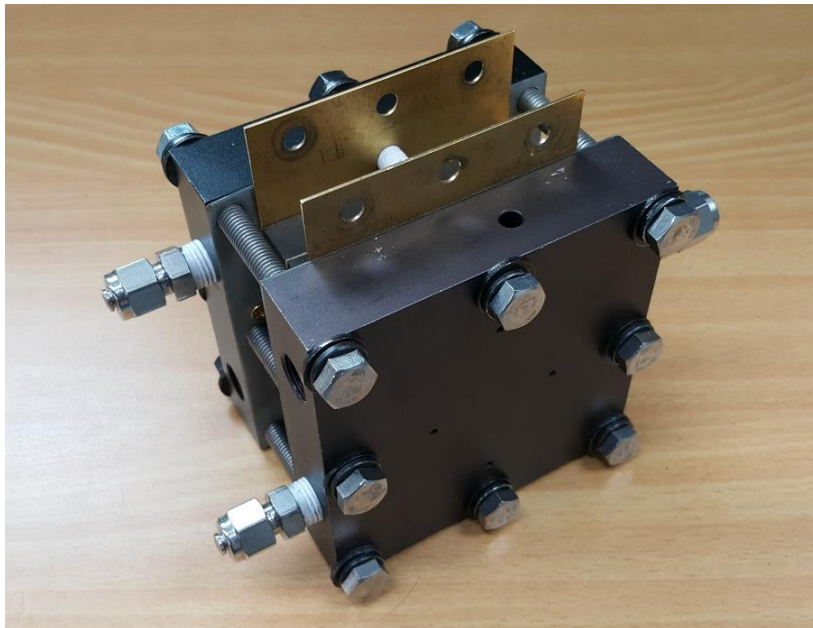


Figure 10. A single PEM unit cell used in model validation experiments

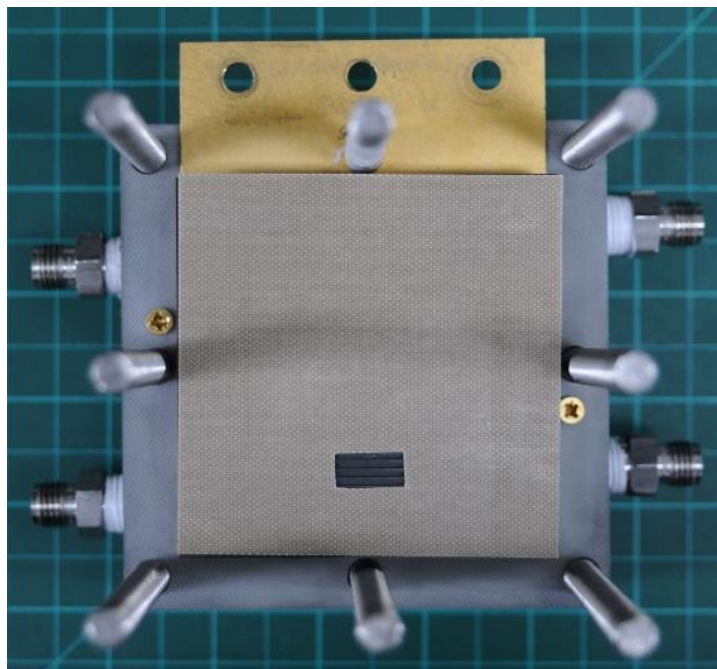
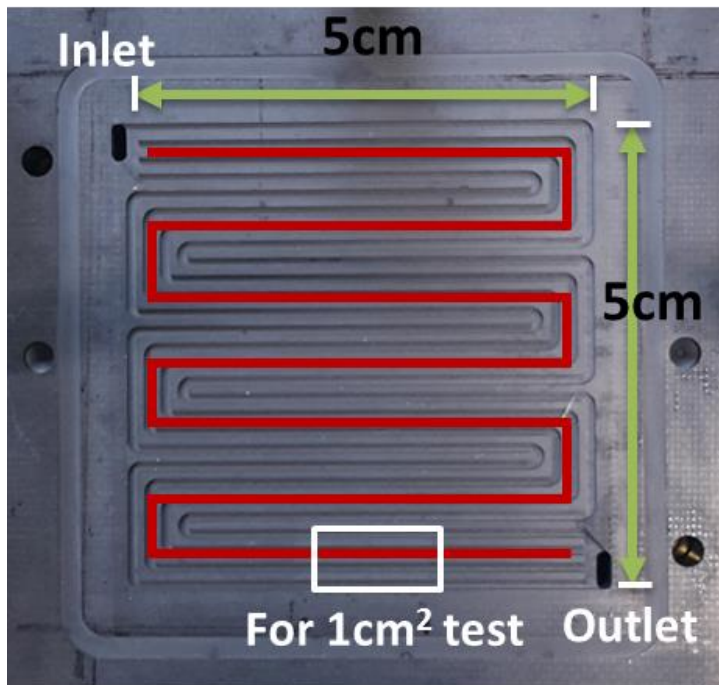


Figure 11.The reduction of effective area using gaskets

3.5. Limiting current density

3.5.1. Experimental conditions

The purpose of the limiting current density test was to obtain the total oxygen transport resistance and isolate the contribution of molecular diffusion resistance from the obtained value. For valid results, the cell needed to be operated in the under-saturation condition. At the same time, a sufficient amount of water vapor was necessary to ensure the limiting current result from mass transport, not from ohmic overvoltage. To achieve this condition, the two-percent oxygen concentration was partially humidified to be used as the inlet gas. Additionally, the active area was reduced to 1cm^2 and the flow rate was set to a high value to minimize the oxygen depletion effect. Two sets of GDLs with the same GORE™ PRIMEA® 5730 MEA were used in this experiments.

Table 6. Experimental condition for limiting current density tests

Parameter	Condition
Test Mode	Voltage Control (1.0V→0.05V, 90 mV/s)
Active Area	1cm^2 (1.4 cm by 0.715 cm)
No. Parallel channel	4
Temperature / Pressure	65 °C / 1atm.
Relative humidity	90 %
Oxygen Concentration	2 %
Diluent gas	Nitrogen / Helium
Flow Rate	0.2 / 2.54 LPM (Anode/Cathode, SR>10)
GDL	GDL A / GDL B
MEA	GORE™ PRIMEA® 5730

3.5.2. Theory

The total oxygen transport resistance can be mathematically expressed as:

$$R_{O_2}^{Total} = (C_{O_2,ch} - C_{O_2,Pt})/N_{O_2} \quad (3.1)$$

Unfortunately, the measurement of neither oxygen concentration at a platinum surface nor an oxygen transport rate is not readily available. However, at limiting current density, the oxygen concentration on the platinum surface becomes zero, and the oxygen transport rate matches the oxygen consumption rate. Then, by equating oxygen transport rate and oxygen reduction rate, total mass transport resistance can be obtained using Eq. (3.2).

$$R_{O_2}^{total} = \frac{4F \cdot C_{O_2}^{ch}}{i_{lim}} = \frac{4F \cdot x_{O_2}^{dry} \cdot (p_T - r_h \cdot p_w^v)}{R \cdot T \cdot i_{lim}} \quad (3.2)$$

Using modestly humidified low oxygen concentration gas with the small active area, it can avoid any liquid water droplet formation or water film over agglomerate. At this specific condition, by changing the diluent gas from nitrogen to helium, it is possible to solely alter the molecular diffusion resistance while holding the other resistance in the same value. As a result, molecular diffusion resistance can be extracted from the total resistance using Eq. (3.3) and Eq. (3.4) [25].

$$R_{O_2-N_2}^{total} - R_{O_2-N_2}^{MD} = R_{O_2-He}^{total} - R_{O_2-He}^{MD} \quad (3.3)$$

$$R_{O_2-N_2}^{MD} = (D_{O_2-He}/D_{O_2-N_2})R_{O_2-He}^{MD} \quad (3.4)$$

The comparison of limiting current results from simulation and experiments can validate the model's ability in estimating total and molecular diffusion resistances.

3.5.3. Limiting current density

Unit cells with an active area of 1cm^2 were prepared with GDL A and GDL B. From experiments, limiting current densities were obtained for the following two cases:

1. Two-percent oxygen with nitrogen base, and
2. Two-percent oxygen with helium base

The limiting current density results for both experiments and simulations are presented in Table 7. The results indicated the minor difference of up to 0.009 A/cm^2 in current density, leading to only 1.63% error.

As mentioned before, the total oxygen transport resistance and the contribution of molecular diffusion resistance were obtained using the difference in limiting current density of two different inert gases. The contributions of molecular diffusion resistance are shown in Figures 12 and 13. The simulation results matched the experimental results with the maximum error of 3.3% in predicting oxygen transport contribution. Therefore, it was reasonable to presume that the model is capable of adequately estimating the oxygen transport resistance in the under-saturated condition. To further validate the model at a saturation condition, current-voltage curves were drawn and compared in the following section.

Table 7. Limiting current density results

Diluent Gas	GDL A		GDL B	
	N2	He	N2	He
Experiment (A/cm ²)	0.441	0.604	0.375	0.536
Simulation (A/cm ²)	0.441	0.601	0.378	0.527
% Error	0.01%	0.44%	0.93%	1.63%

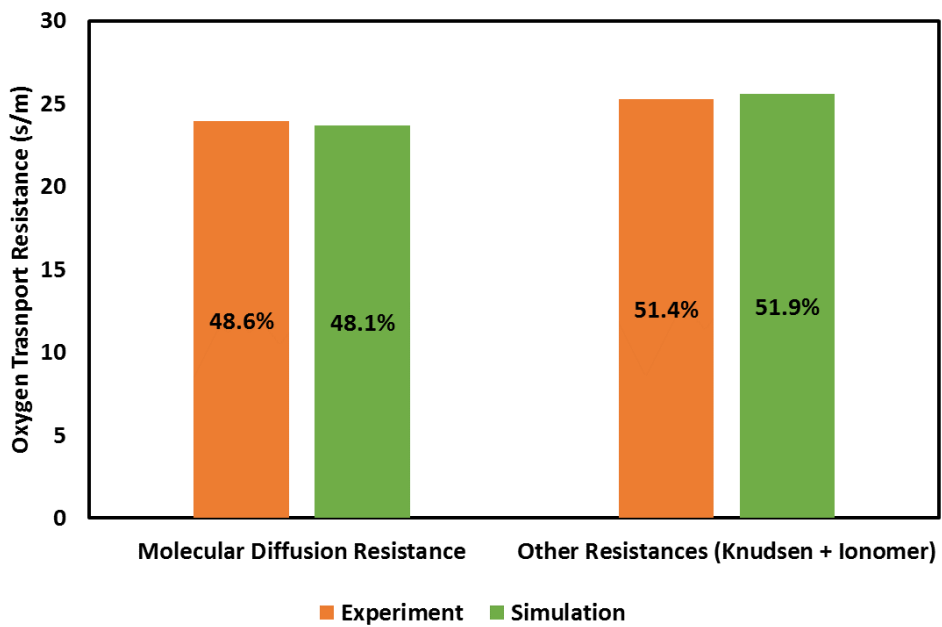


Figure 12. Comparison of molecular diffusion resistance and other resistances between simulation and experiment (GDL A)

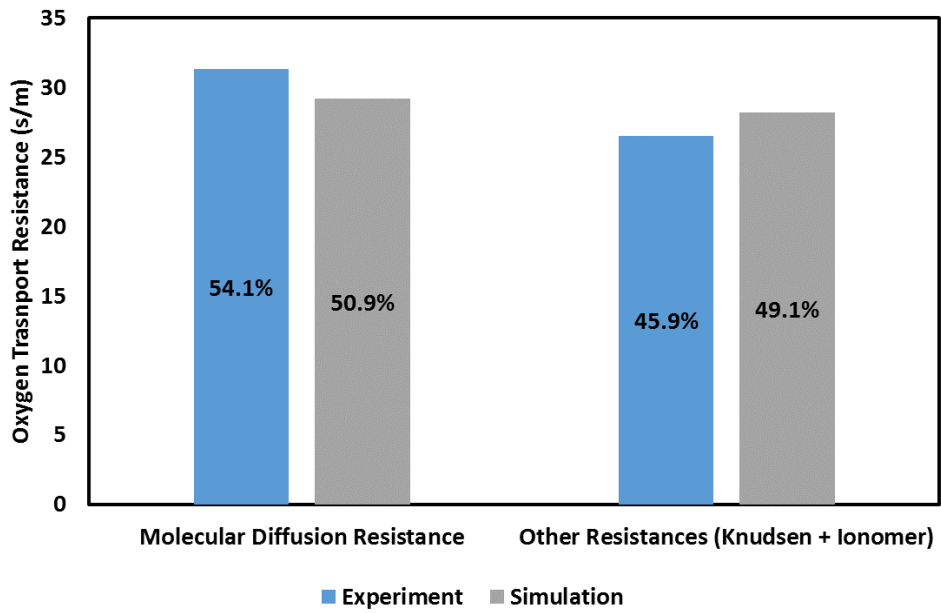


Figure 13. Comparison of molecular diffusion resistance and other resistances between simulation and experiment (GDL B)

3.6. Polarization curves

Single unit cells with an active area of 25cm² were tested to obtain polarization curves. For simulation data, a quasi-three-dimensional model was modeled to capture the spatial variation in gas composition along the channel. The polarization curves were obtained from both experiments and simulation to compare and validate the model. Figures 13 and 14 show the comparison of polarization curves between simulation and experiment of both GDLs. There were slight voltage deviations between simulation and experiment up to 0.4 A/cm² for GDL A case. However, this error was limited to the low current density region, and it disappeared as the current density increased. Overall, the model was capable of simulating the PEM appropriately.

Table 8. Experimental condition for polarization curves

Description	Value
MEA	GORE PRIMEA™ 57® Series
GDL	GDL A / GDL B
Active Area	25 cm ²
Operating Temperature	65 °C
Relative humidity	100 %
Inlet Gas	Pure hydrogen (Anode) / Air (Cathode)
Stoichiometric Ratio	1.5 (Anode) / 2 (Cathode)

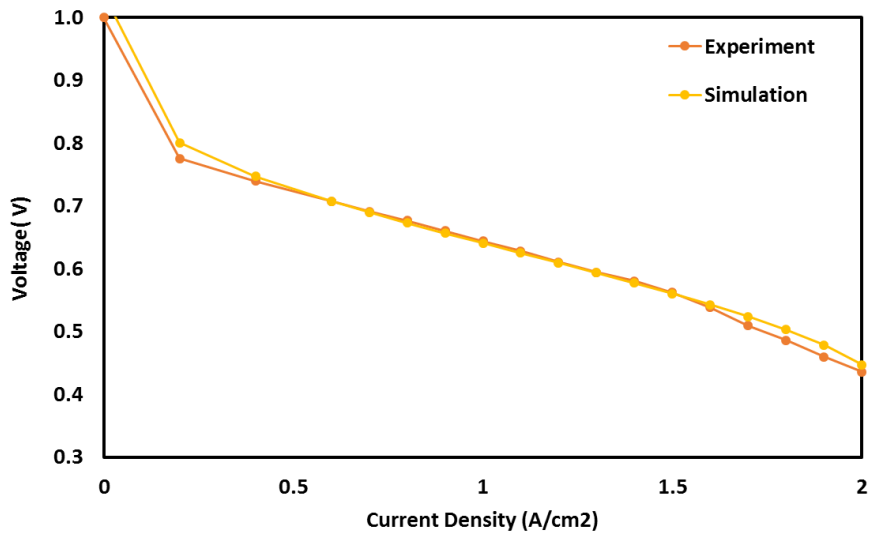


Figure 14. Comparison of experimental polarization curve and simulated polarization curve (GDL A)

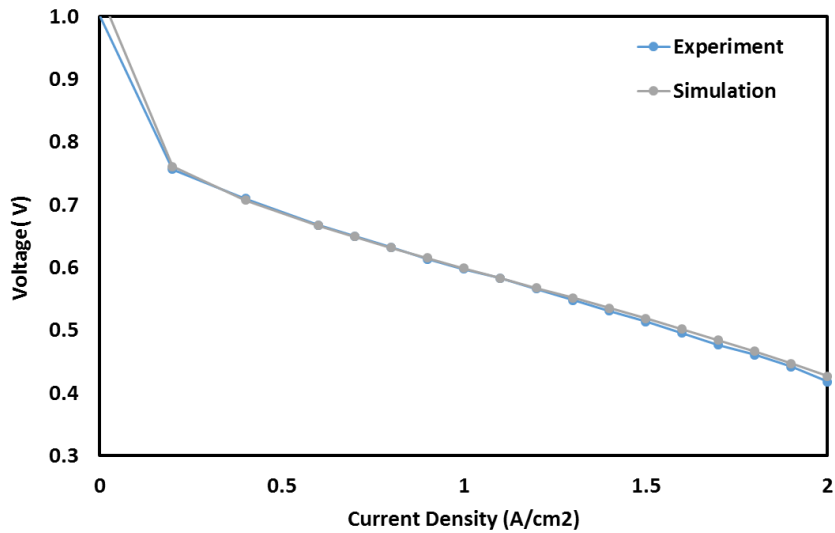


Figure 15. Comparison of experimental polarization curve and simulated polarization curve (GDL B)

Chapter 4. Results and Discussion

In this chapter, the individual oxygen transport resistances were obtained using the developed model. Two different GDLs with distinct physical properties were adapted to the model parameters to observe the change in specific oxygen transport resistance for each case. For operating conditions, two specific conditions were chosen. Firstly, the same condition as the previous limiting current validation was selected to further separate the empirically obtained oxygen transport resistance. Secondly, a normal air operating condition was chosen. In this case, the inlet gas was fully humidified to promote the condensation of generated water. The model simulated the oxygen transport resistance of each component even at the saturated condition.

4.1. Under-saturated condition

In the previous chapter, the total transport resistance and the contribution of molecular diffusion and Knudsen diffusion of a whole cell were empirically obtained using limiting current density. The separation of the molecular diffusion was done as a whole cell, and further separation of the transport resistance would require a number of carefully planned experiments. Fortunately, the developed model easily overcame this barrier and provided the detailed information on the oxygen transport resistance. Two sets of GDLs, namely, GDL A and GDL B were simulated to observe the change in transport resistance, and the results provided the intrinsic structural resistance on each component.

4.1.1. Limiting current density

4.1.1.1. GDL A

The oxygen transport resistance was divided into channel resistance, substrate resistance, MPL resistance and catalyst layer resistance. The catalyst layer resistance was further separated into the gas-phase diffusion catalyst layer resistance and the ionomer permeation resistance. In addition, the contribution of molecular resistance and Knudsen resistance were obtained for the MPL and the catalyst layer.

Channel-GDL interface transport resistance was 7.2 s/m, and the substrate transport resistance was 10.1 s/m. The MPL showed the highest resistance of 17.7 s/m which was consisted of 25% molecular diffusion resistance and 75% of Knudsen diffusion resistance. At the catalyst layer, molecular resistance and Knudsen resistance contributed 1.2 s/m and 4.2 s/m, respectively. Lastly, the ionomer resistance, including the oxygen permeation resistance was 8.9 s/m. Using the developed model, the total oxygen transport resistance of 49.3 s/m was divided into individual oxygen transport resistance.

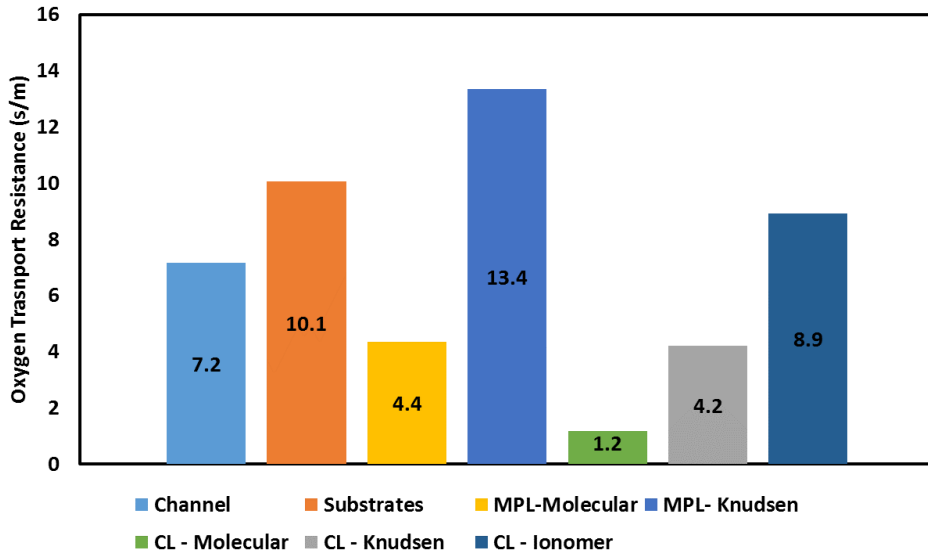


Figure 16. Oxygen transport resistance of each component at under-saturated condition (GDL A)

4.1.1.2. GDL B

In a similar fashion, the model was simulated with GDL B parameter. The total oxygen transport resistance of 57.4 s/m was separated as shown in Figure 17. The channel-GDL interface resistance was the same as before, 7.2 s/m. The substrate resistance was 13.1 s/m, and the MPL resistance was 22.8 s/m. The MPL resistance was additionally divided into molecular diffusion resistance of 6.6 s/m and Knudsen diffusion resistance of 16.2 s/m. The contribution of molecular resistance and Knudsen resistance in the MPL were 29% and 71%, respectively. The resistance of the catalyst layer and the ionomer resistance were 5.4 s/m and 8.9 s/m.

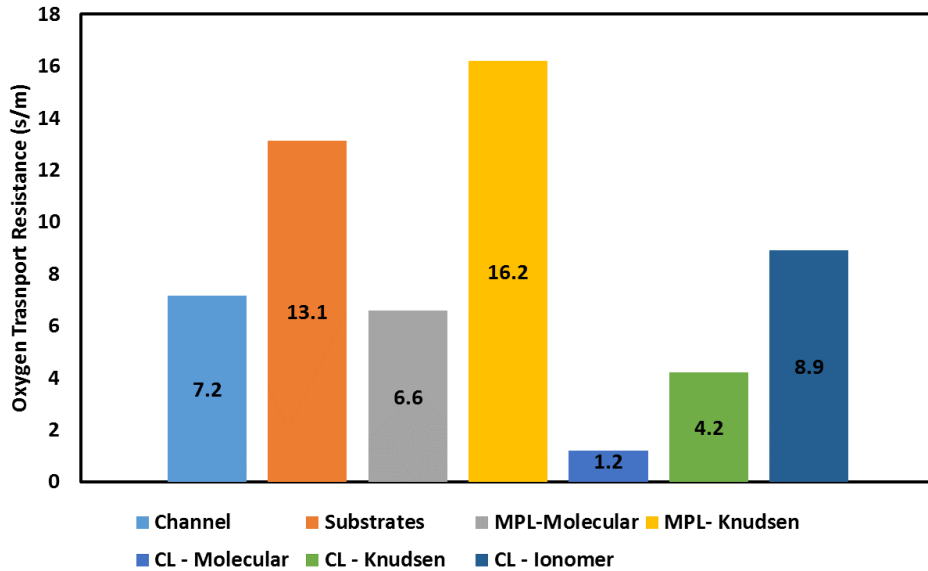


Figure 17. Oxygen transport resistance of each component at under-saturated condition (GDL B)

4.1.1.3. Comparison between A and B

Total oxygen transport resistance was 49.3 s/m for GDL A, and 8.4 s/m for GDL B. The total resistance was 8.4 s/m lower in GDL A; hence GDL A showed a 14% reduction in oxygen transport resistance. The contribution of individual resistance for each case is shown in Figure 18 and 19.

The result indicated that MPL contributed up to 40% of the dry transport resistance. The small scale of MPL pore size with low porosity acted as the major obstacle in oxygen transport. The MPL resistance of GDL A corresponded to 78% of GDL B.

Even though GDL A had a smaller pore size which increases the resistance, the thinner layer thickness had resulted in a smaller MPL resistance. Noticeably, the GDL A showed molecular and Knudsen diffusion resistance ratio of 1:3, while GDL B showed 1:2.46. The reason for the higher ratio of GDL A was from the smaller average pore size.

Meanwhile, channel resistances were around 12~15% of the total resistance and remained at the same resistance of 7.2 s/m. The surface roughness of GDLs influenced the mass transfer between channel and GDL. However, this effect was not considered in the model; hence the value was not changed.

Next, the diffusion in the catalyst layer was responsible for 10% of the total resistance which is a substantial amount, considering its thickness of 7 μm . Therefore, it is advised to sensibly control the water saturation in this layer to maintain the low oxygen transport resistance.

Lastly, the contribution of ionomer resistance was roughly 15%. The majority of the resistance was from the discontinuity in oxygen concentration as oxygen permeated through the ionomer.

Overall, the resistance of GDL A was lower than that of GDL B at the under-saturated condition. The reason for this outcome was derived from the higher porosity of the substrate and thinner MPL thickness, despite the smaller pore size of GDL A.

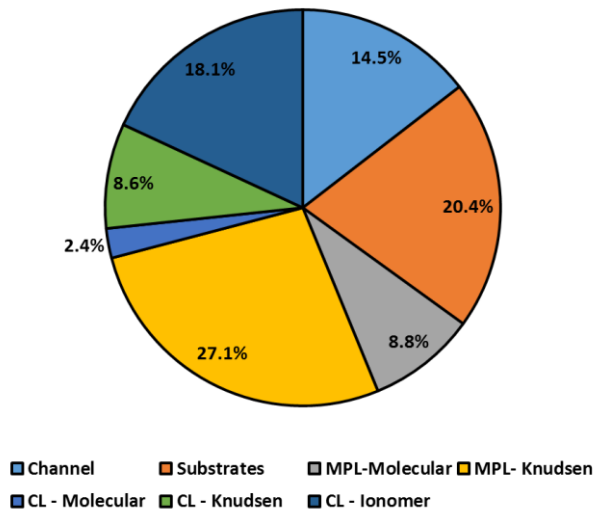


Figure 18. Contribution of individual oxygen transport resistance at under-saturated condition (GDL A)

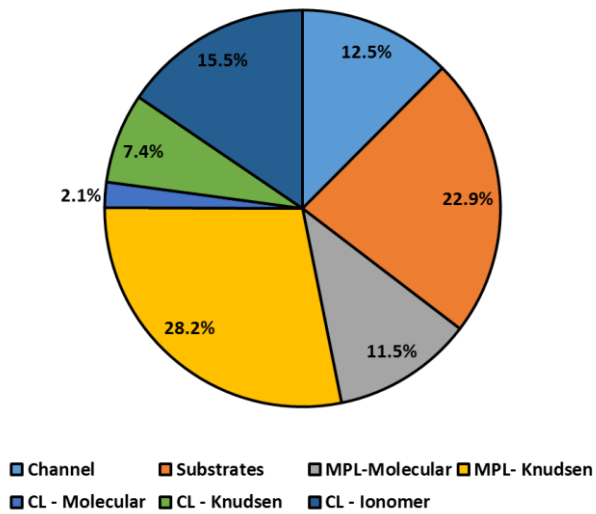


Figure 19. Contribution of individual oxygen transport resistance at under-saturated condition (GDL B)

4.2. Over-saturated condition

A normal operating PEM fuel cell experiences condensation. At the over-saturated condition, the measurement of oxygen transport resistance is empirically elusive. Therefore, the simulated model was implemented to utilize the developed model in analyzing the oxygen transport resistance by each layer.

In the following analysis, the concentration discontinuity at the ionomer surface was not calculated in the ionomer resistance. The concentration discontinuity may lead to a high interfacial resistance at a relatively low current density which may confuse the analysis of individual transport resistance. The phase change occurs for all cases. Therefore, to avoid any confusion and solely observe the change in ionomer film and water film resistance, phase-change resistance was excluded in the calculation of ionomer and water film resistance.

4.2.1. 1 A/cm² vs. 2 A/cm²

Two operating points were arbitrary selected to examine the transport of oxygen. The intermediate current density of 1 A/cm² and high current density of 2 A/cm² were chosen to observe the resistance under a minor load condition and a heavy load condition.

4.2.1.1. GDLA

Figure 20 shows the total oxygen transport resistance at 1 A/cm² and 2 A/cm². The total oxygen transport resistance increased from 46.03 s/m to 52.03 s/m. The total resistance increased by 13% as the current density doubled. Similar to the under-saturated condition, the resistance in the MPL was the most dominant resistor, and their values were 18.24 s/m for 1 A/cm² and 18.37 s/m for 2 A/cm². Noticeably, the diffusion resistance in the catalyst layer rose by 6.08 s/m, from 9.02 s/m to 15.10 s/m. Therefore, the majority of the increased resistance was from this layer. Meanwhile, due to the increased in water saturation at the catalyst, the water film resistance increased by 0.05. Meanwhile, no obvious changes were observed in the ionomer, substrate and channel resistance.

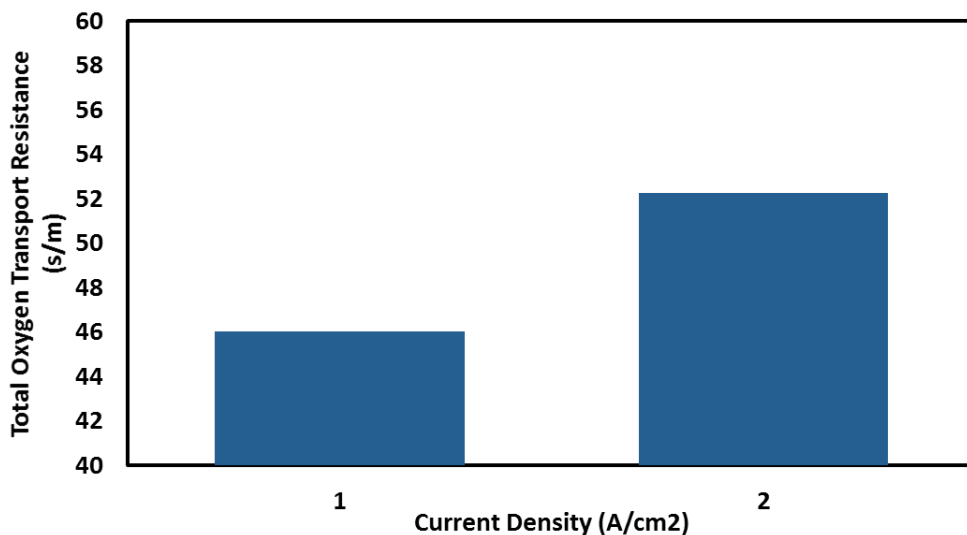


Figure 20. Total oxygen transport resistance at 1 A/cm² and 2 A/cm² (GDL A)

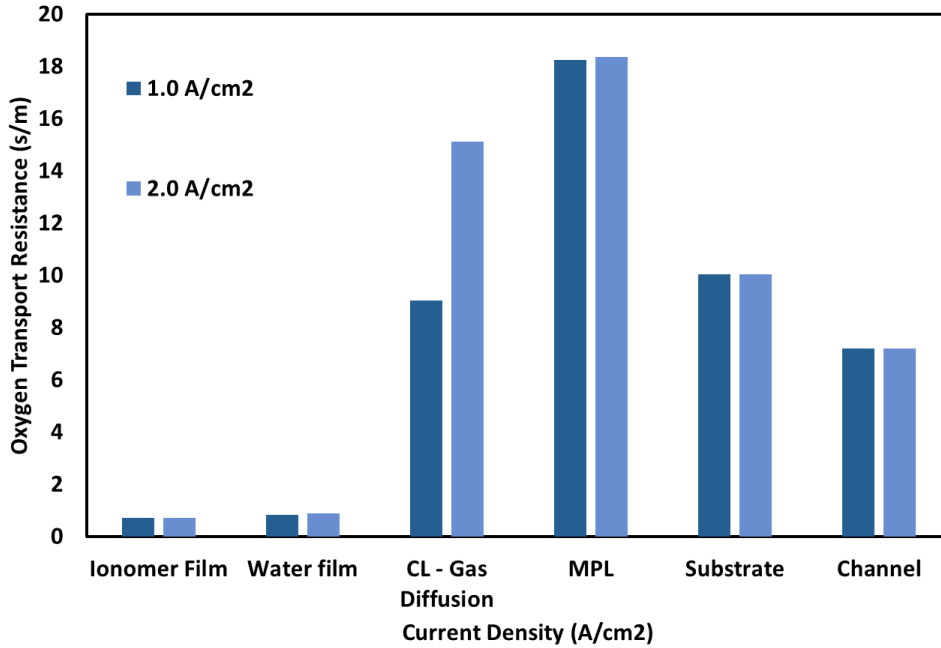


Figure 21. Individual transport resistance at 1 A/cm² and 2 A/cm² (GDL A)

4.2.1.2. GDL B

The simulation results for GDL B indicated the increase of 0.64 s/m in the total transport resistance. The total resistance was initially 51.68 s/m at 1 A/cm² and it grew 1% (52.32 s/m) as the current density doubled. A high portion of resistance was from the MPL, and it showed the highest shifts of 0.37 s/m. The second noticeable change was from the catalyst layer which resulted in 0.19 s/m increase. The water film resistance and substrate resistance the increased by 0.07 s/m and 0.02 s/m, respectively.

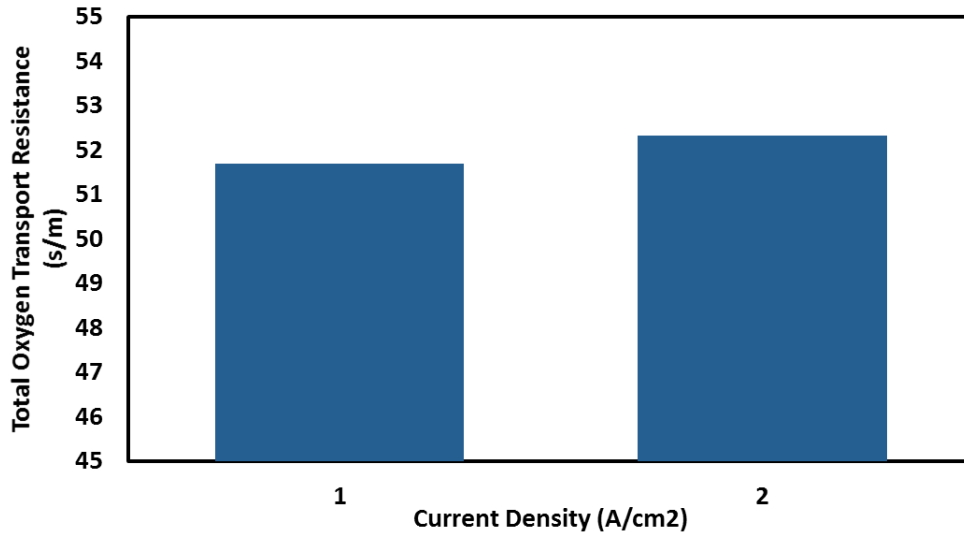


Figure 22. Total oxygen transport resistance at 1 A/cm² and 2 A/cm² (GDL B)

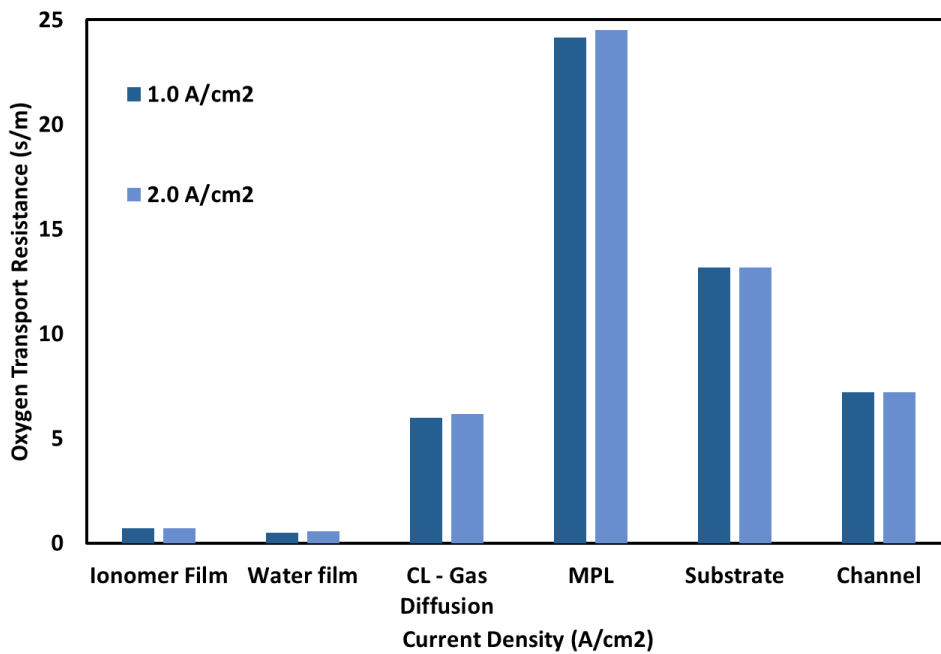


Figure 23. Individual transport resistance at 1 A/cm² and 2 A/cm² (GDL A)

4.2.1.3. Comparison

The total oxygen transport resistance of GDL A was 5.65 s/m lower than GDL B at 1.0 A/cm². However, when the current density doubled, the total resistance became almost the same as GDL B. According to the pie charts, the contribution of the catalyst layer for GDL A substantially increased from 19.6 % to 28.9 %, while GDL B showed a minor change of 0.2%. The water saturation profile revealed that GDL had a tendency of holding water at the catalyst layer. By contrast, GDL B showed a propensity of lowering catalyst layer saturation by distributing the liquid water all over GDL. Therefore, substrate and MPL saturation of GDL B were higher than A

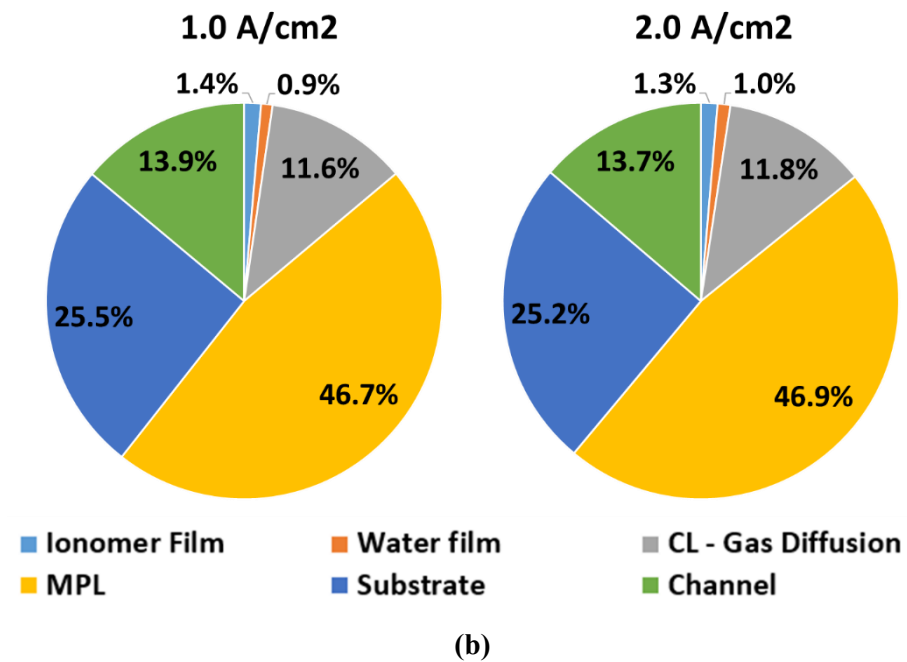
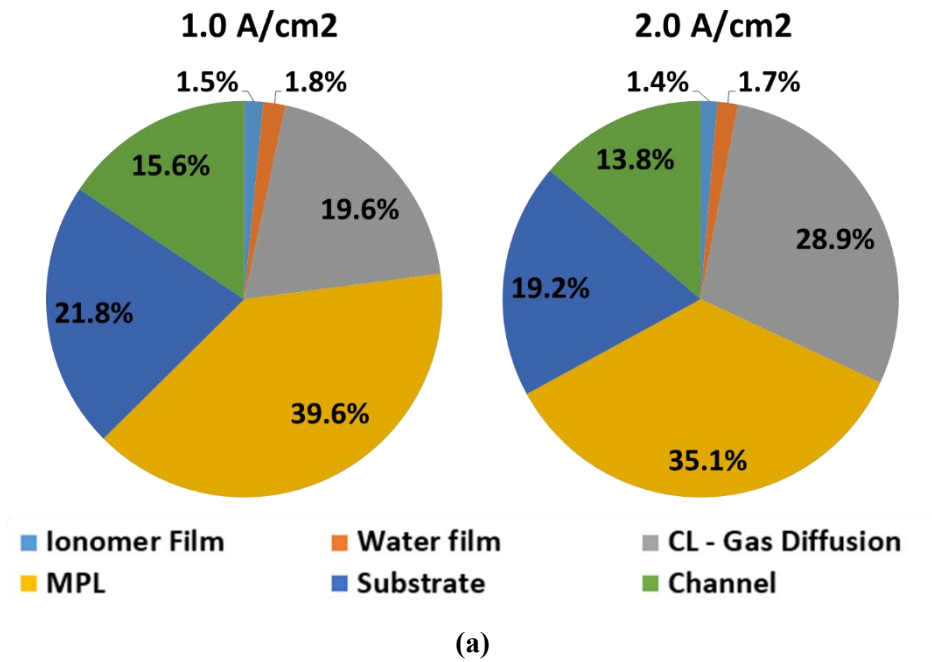
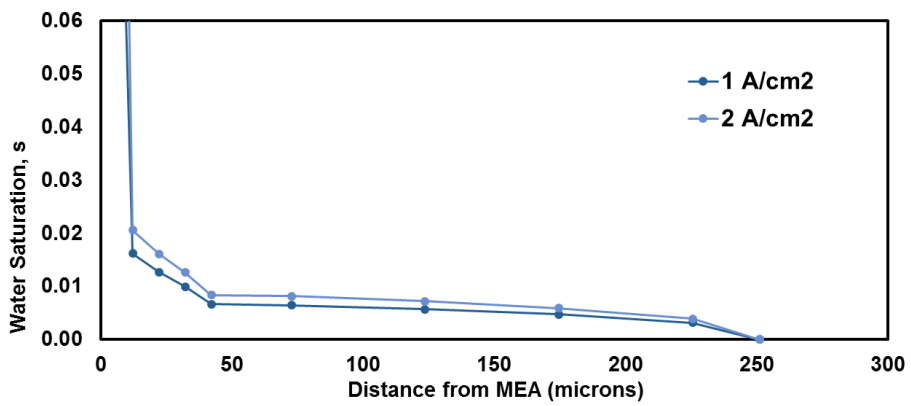
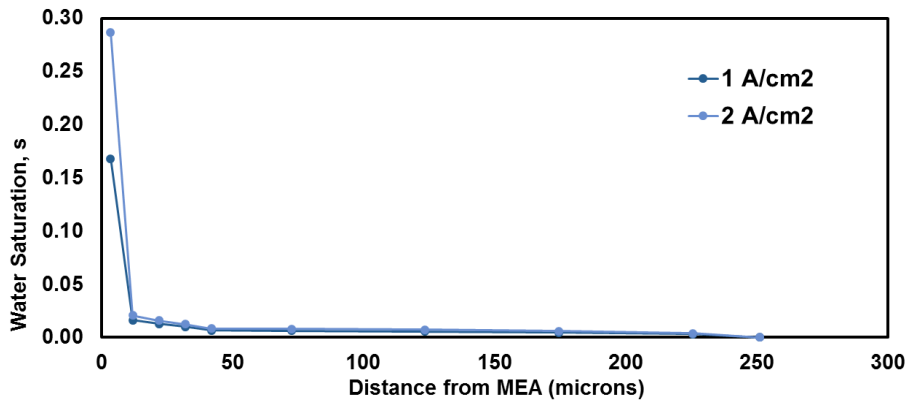
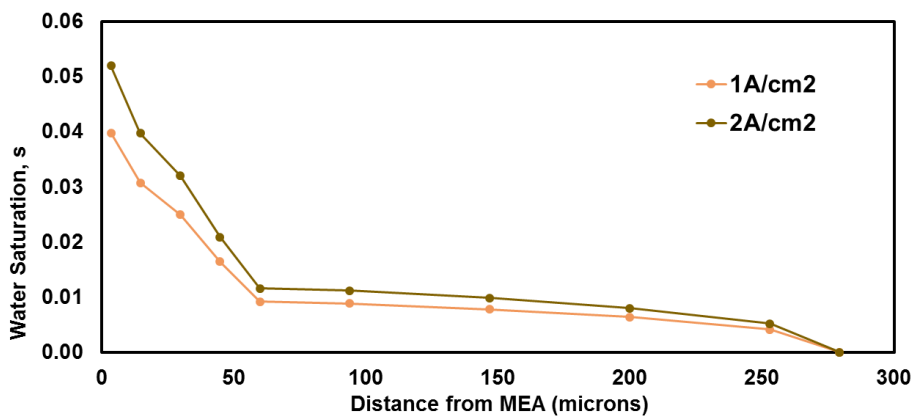


Figure 24. Contribution of individual resistance at 1A/cm² and 2 A/cm² for
a) GDL A, b) GDL B



(a)



(b)

Figure 25. Water saturation profile at 1 A/cm² and 2 A/cm² for a) GDL A, b) GDL B

4.2.2. Oxygen transport resistance trends

With the developed model, the trends of individual oxygen transport resistance were analyzed by varying operating current density from 0.4 A/cm^2 to 2.0 A/cm^2 at a relative humidity of 100%. The water production rate is directly proportional to the current density. Hence, the amount of condensed water and the water-filled pore volume increases as current density increases, leading to the growth in the transport resistance. However, the susceptibility of the cell differs from cell to cell. In this study, GDL A and GDL B were chosen to observe the difference.

4.2.2.1. GDL A

A cell with GDL A showed a sizeable increase of 19.7% in the total oxygen resistance as current density quadrupled (43.65 s/m at 0.4 A/cm^2 to 52.27 s/m at 2.0 A/cm^2). Figure 21 shows the trends of transport resistance of each component according to the current density. It was found that the catalyst layer resistance doubled from 6.97 s/m to 15.1 s/m . Meanwhile, water film and MPL increased 23.8% and 1.8%, respectively, however, the increase in the resistance were relatively small to come to any significant effect on the total transport resistance. Noticeably, ionomer resistance slightly decreased 1% due to the temperature increase, caused by an excessive heat generation.

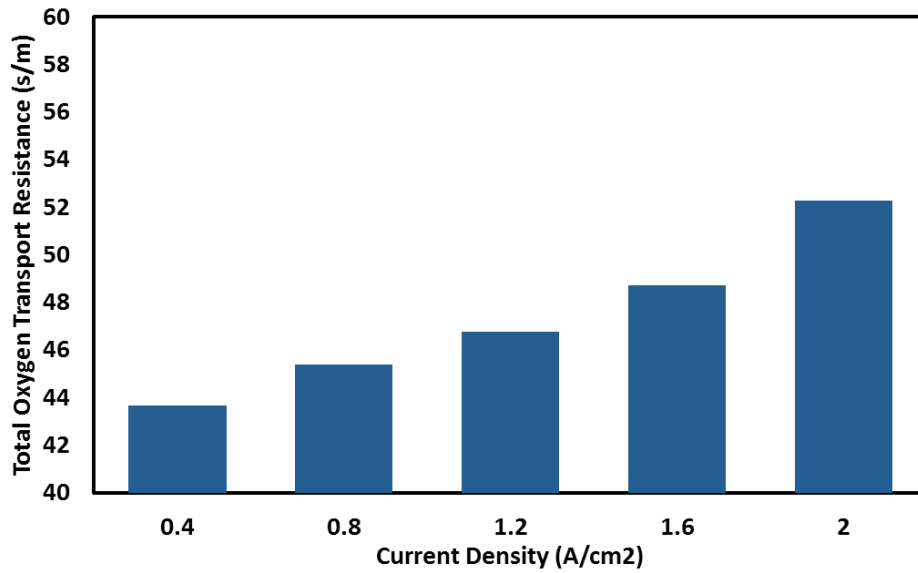


Figure 26. Total oxygen transport resistance of GDL A

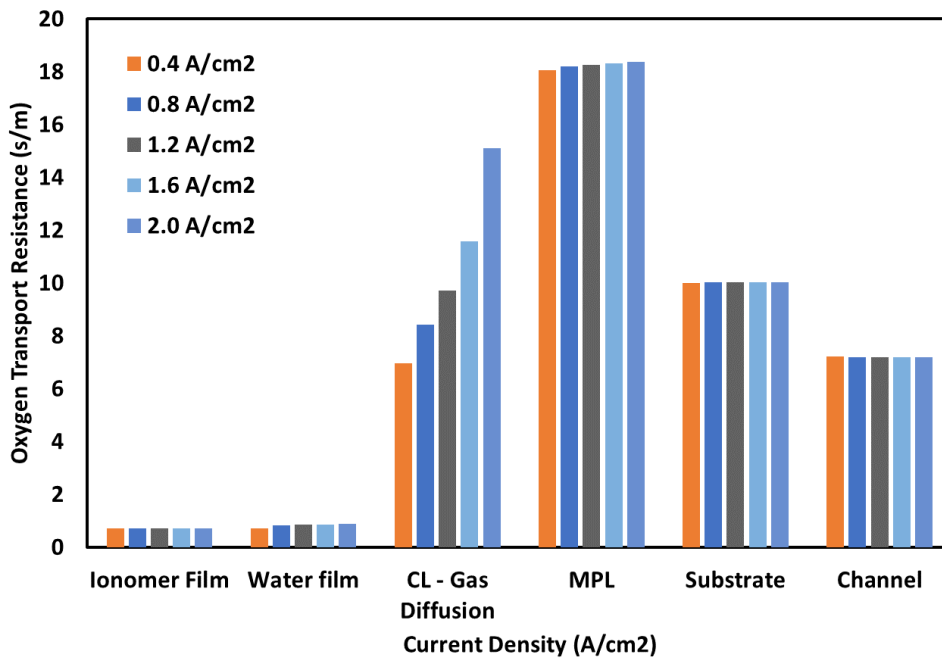


Figure 27. The change in individual oxygen transport resistance between 0.4 A/cm² to 2.0 A/cm² (GDL A)

4.2.2.2. GDL B

GDL B also exhibited similar trends. Due to the condensation of product water, the oxygen transport resistance increased 3 % from 50.4 s/m at 0.4 A/cm² to 52.3 s/m at 2.0 A/cm². The resistance of the catalyst layer increased from 5.77 to 6.17s/m, which corresponds to 7.1% increase. The MPL also showed the increase of 3.8% (23.63 at 0.4A/cm² to 24.52 s/m at 2.0A/cm²). The water film resistance showed the highest percentage of the increase, 50%. Nevertheless, the effect was only 0.18s/m which was less than 1% of the total resistance.

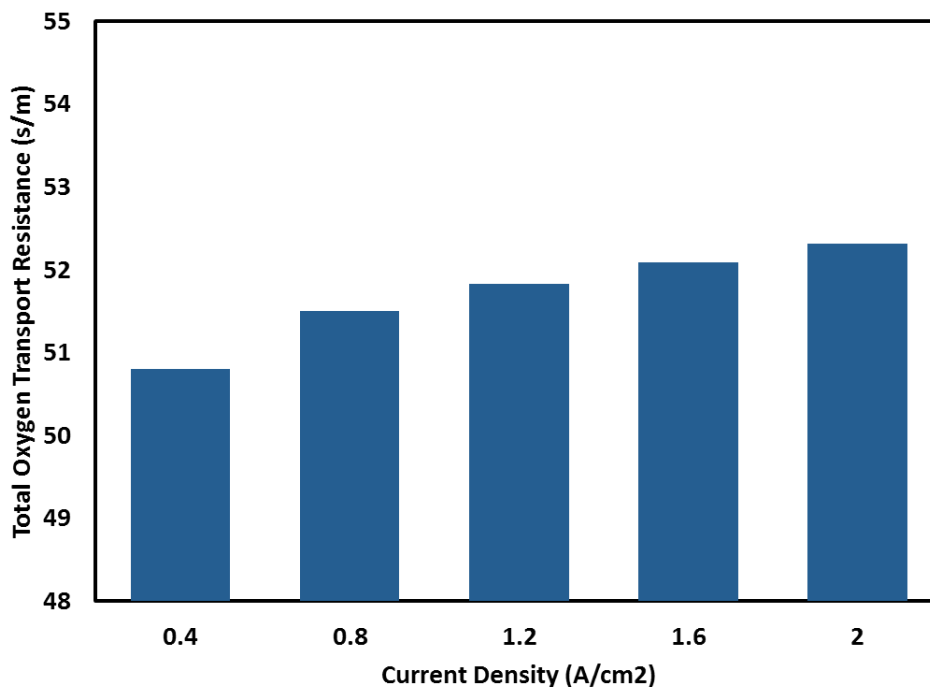


Figure 28. Total oxygen transport resistance of GDL B

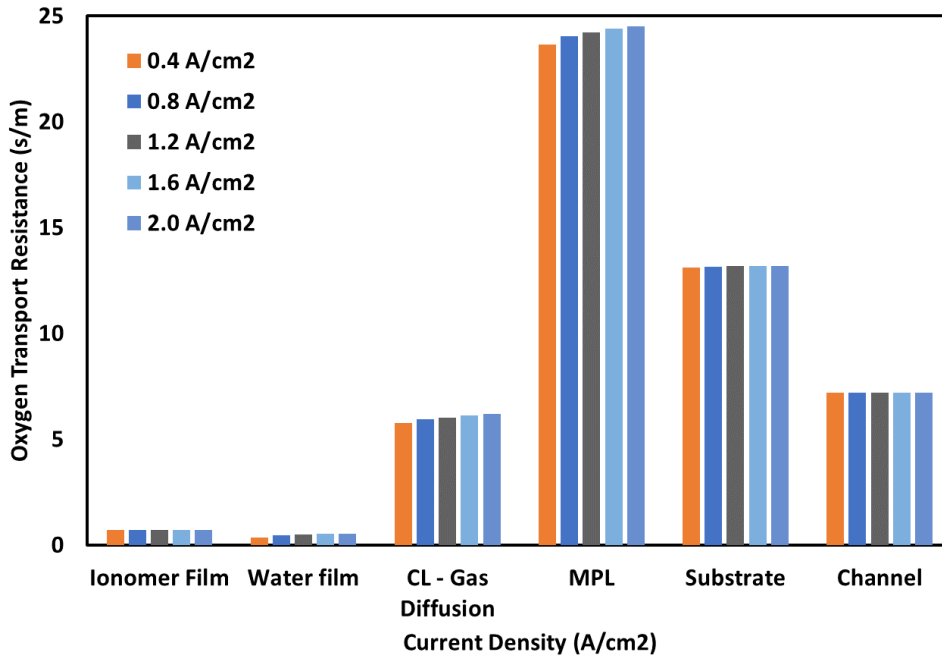


Figure 29. The change in individual oxygen transport resistance between 0.4 A/cm² to 2.0 A/cm² (GDL B)

4.2.2.3. Comparison between A and B

GDL A showed a lower oxygen transport resistance at the low current density region, as it showed the lesser oxygen transport resistance in the dry condition. The total oxygen transport resistance was increased with an increasing current. However, the degree of the slope was different as shown in figure 30. It demonstrated that the GDL A was initially 7.15 s/m lower at 0.4 A/cm², but only 0.05 s/m lower at 2.0A/cm². The transport resistance of GDL A increased faster than that of GDL B.

The ionomer resistance remained the same for both cases as the same MEA was simulated, and it showed no visual change according to the current density (Figure 31). There was a change in the water film resistance between two samples. Figure 32 showed the water film thickness according to the current density and its resistance. Due to the increased condensed liquid water, water film thickness increased as the current density increased. GDL A had a thicker water film; hence a higher resistance. Also, the increase in water film thickness was faster in GDL A. However, the resistance of water film was only 1~2% of the total resistance, and this was not significant.

The increase of the oxygen transport resistance of GDL A was originated from the catalyst layer. GDL A was initially 6.96 s/m which was slightly higher than GDL B. At 2.0A/cm² resistance of GDL A reached 15.1 s/m which is the 117% increase of the previous value. While the GDL B holds relatively steady value, MPL, GDL, and channel show almost no larger changes of 1% of the total resistance.

Figure 37 indicates the overvoltage of each cell. It was found that GDL A had a lower activation loss due to the lower oxygen transport resistance. However, at near 2.0A/cm², it started to show a faster increase as the catalyst layer resistance increased. At the same time, GDL A showed a slightly lower ohmic resistance due to high water content at the membrane. However, its effects were minor as the reactant gases were fully humidified.

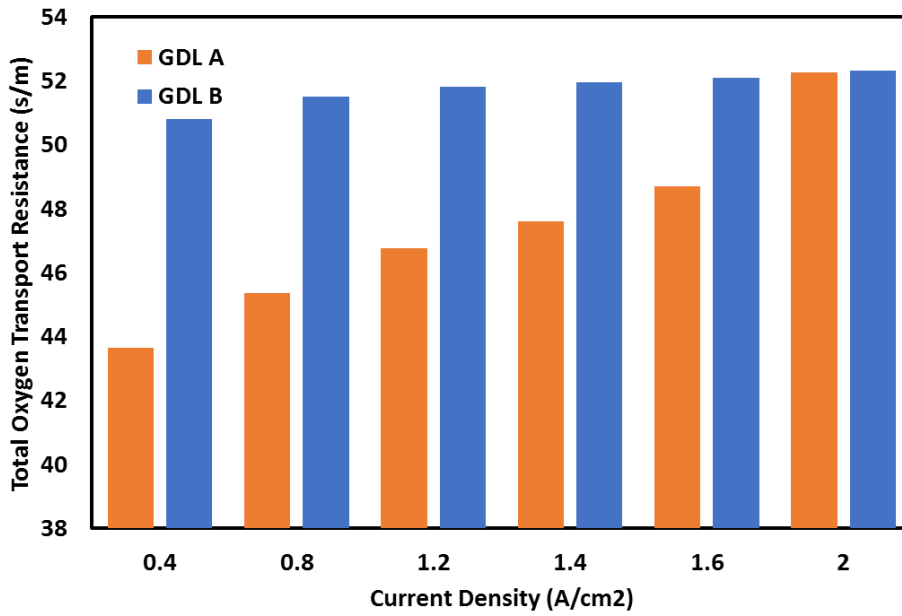


Figure 30. Total oxygen transport resistance under various operating current densities.

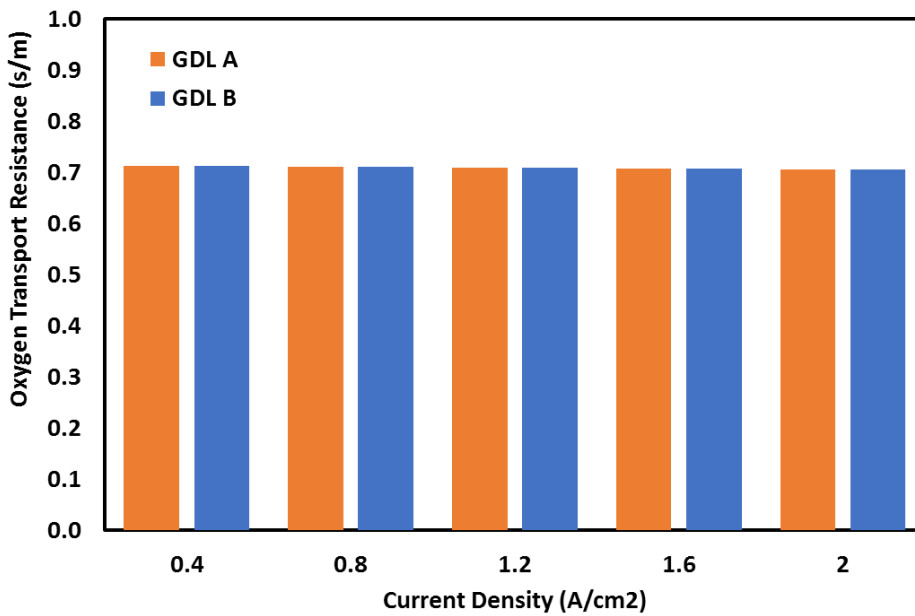


Figure 31. The change in ionomer resistance under various current densities

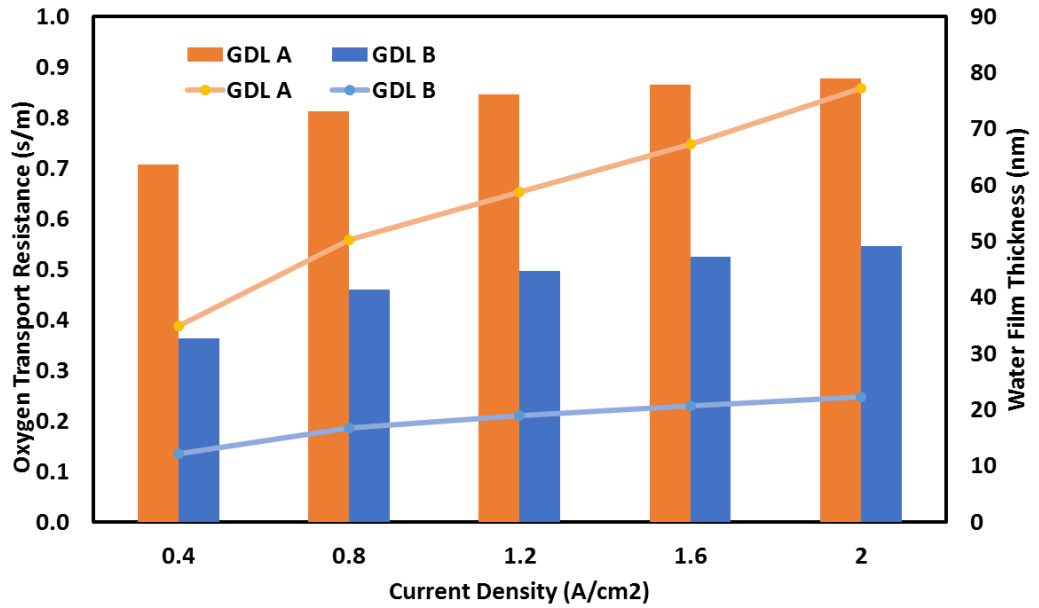


Figure 32. The change in water film resistance and water film thickness under various current densities

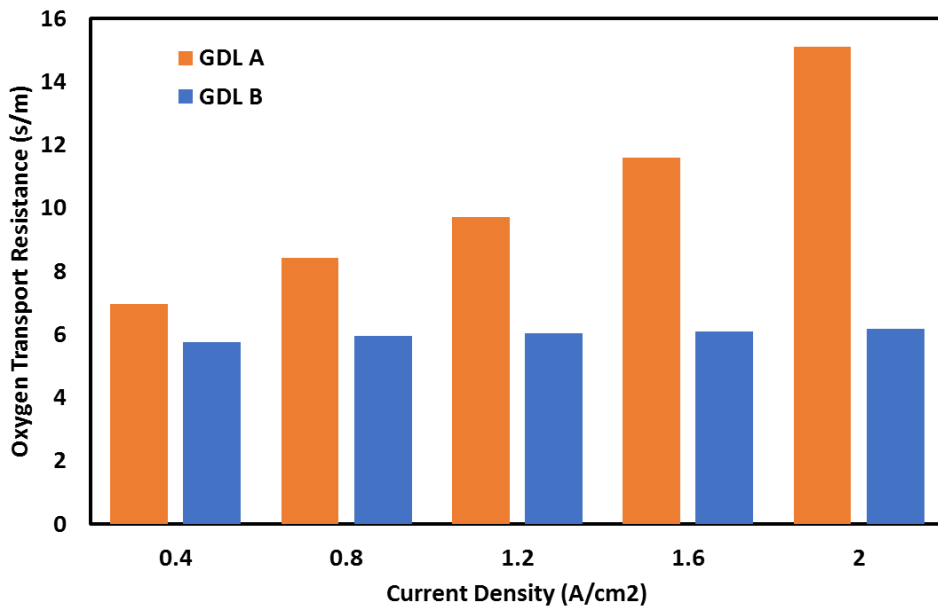


Figure 33. The change in catalyst layer resistance under various current densities

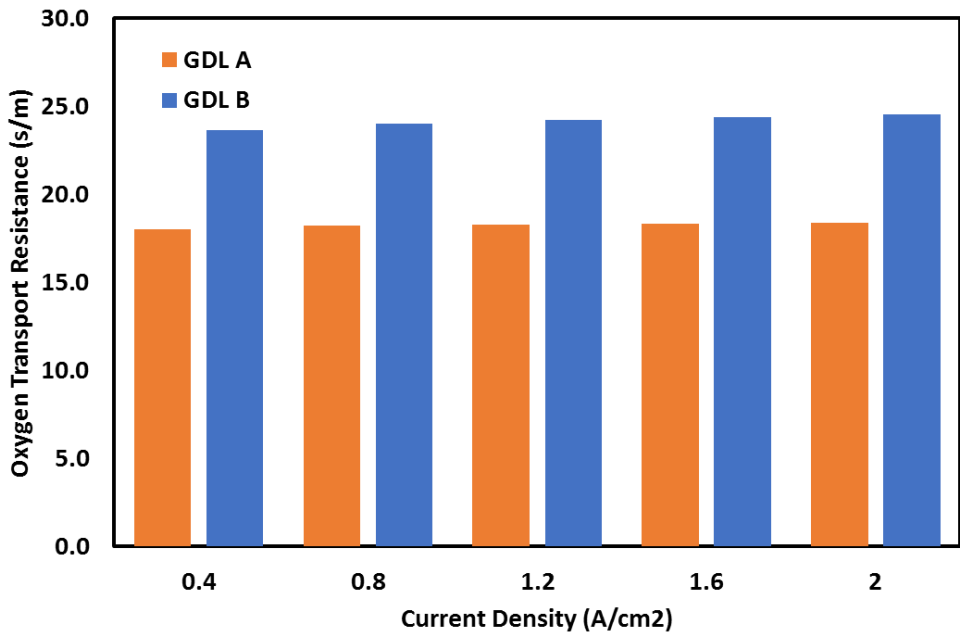


Figure 34. The change in MPL resistance under various current densities

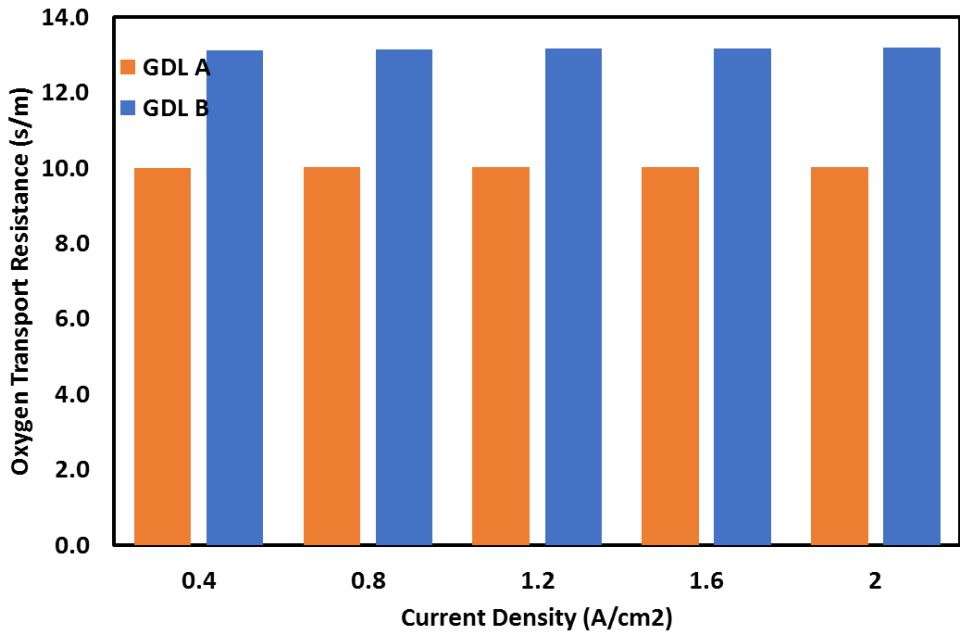


Figure 35. The change in substrate resistance under various current densities

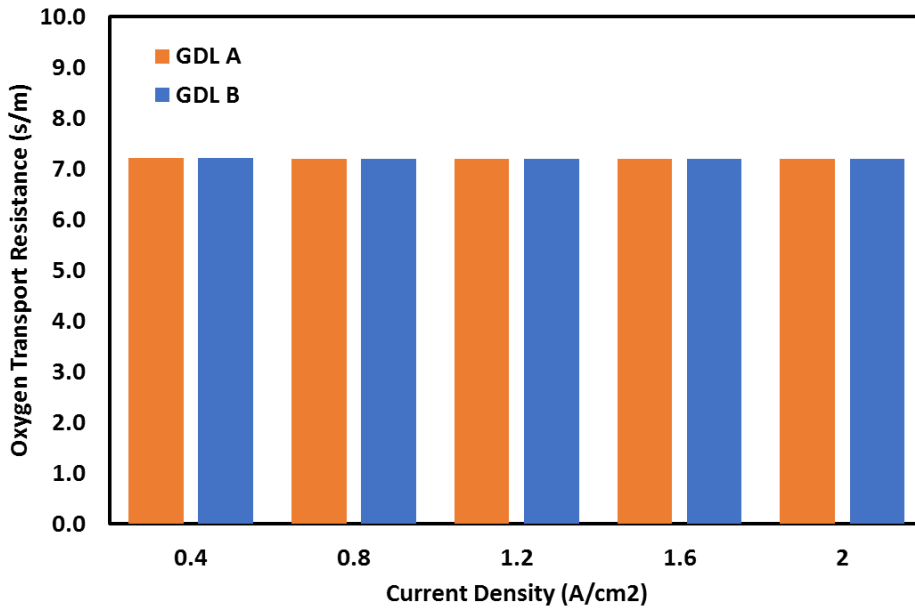


Figure 36. The change in channel resistance under current densities

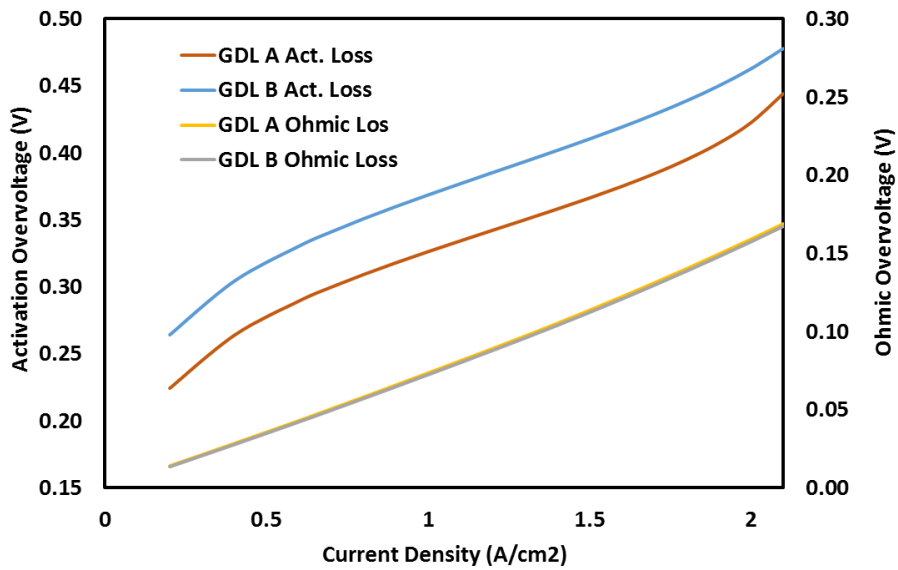


Figure 37. Comparison of activation overvoltage and Ohmic overvoltage obtained from simulation

4.3. Further discussion

The model was simulated to separate the oxygen transport resistance at both under-saturated condition and over-saturated condition. Running the simulation at the under-saturated condition provided an intrinsic structural transport resistance. On the other hand, running the simulation at the over-saturated condition projected the oxygen transport resistance of the standard PEM fuel cell condition.

The advantage of this model was the ability to observe the oxygen transport resistance for each control volume. In addition, the contribution of both Knudsen diffusion and Molecular diffusion could be isolated. Moreover, the change in the oxygen transport resistance along the channel could be obtained, even though the values were averaged in this paper.

However, with this model, there are some difficulties finding the correct model parameters for satisfactorily predicting the oxygen transport resistance. In order to adequately describe the oxygen transport phenomena, a number of properties of GDL and catalyst layer such as contact angle, permeability, average pore size, and porosity should be measured. In this study, a number of properties had to be conjectured using published research paper due to difficulties involved in measuring all parameters.

In this model, the intra-agglomerate oxygen transport resistance was not reflected. This may result in errors in simulating a gradual increase in concentration overvoltage. Therefore, the modeling of the diffusion inside the agglomerates is required in the future

The two GDL samples were analyzed at the fully humidified condition. The both simulation and experimental results indicated that the GDL A is superior to GDL B. Noticeably, GDL A had a tendency of holding liquid water near the catalyst layer. This unique property was not advantageous at the fully humidified condition, but considering the real operating condition of a PEM fuel cell, which is partially humidified, GDL A would show a superior performance by maintaining a lower ionic resistance.

Chapter 5. Conclusion

An existing quasi-three-dimensional model of PEMFC is developed to analyze the oxygen transport resistance under various operating conditions. The following changes to the previous model were made to more accurately estimate the oxygen transport phenomenon.

- 1) Multicomponent diffusion
- 2) Knudsen diffusion, and
- 3) Spherical agglomerate structure

The developed model was validated with two different sets of GDLs, namely GDL A and GDL B. The validation process was conducted in two steps. Firstly, the limiting current density of two percent oxygen gas, using two different diluent gas, nitrogen, and helium, were compared. The model passed the first validation with only 0.45% error in limiting current density. This ensures its ability to adequately estimate the total oxygen transport resistance and the contribution of the molecular diffusion resistance from other resistances such as Knudsen and ionomer resistance. For the second validation, the polarization curve was obtained and compared with the experimental result. Except for small deviation near open circuit voltage, the overall simulation results matched well with the experiments.

In this model, a number of assumptions on the physical property of the catalyst layer such as the number of agglomerate, radius of the agglomerate and the ionomer thickness were made. Even though this may result in the incorrect response of the system, the voltage response of the cell agreed well with corresponding experiments.

The developed model was utilized to observe the oxygen transport resistance of two sets of GDLs under various operating points. It was found that, as the current density rises, the oxygen transport resistance increases. The additional resistance is mainly from the formation of thicker water film and the higher diffusion resistance at a catalyst layer due to the increase in water saturation. The simulation results indicated that the oxygen transport resistance of GDL A is smaller than that of GDL B. However, the GDL A had a tendency of holding water near the catalyst layer and resulted in the faster increase in total transport resistance with the current.

Overall, the model was able to investigate the transport resistance of two different sets of GDL.

In conclusion, the developed model was able to investigate the individual oxygen transport resistance in a PEM fuel cell under various operating conditions. The model was also able to capture the impact on individual oxygen transport resistance due to the change in GDL properties. The model shows a great potential in evaluating the individual components of the cell.

Chapter 6. Bibliography

- [1] U.S. Climate Action Report. In: State USDo, editor.2014.
- [2] Thompson GJ. In-Use Emissions Testing of Light-Duty Diesel Vehicles in the United States. West Virginia University; 15 May 2014.
- [3] Riley C. Mitsubishi : We've been cheating on fuel tests for 25 years. CNN Money; 2016.
- [4] Hamada N, Goto S, Seiji S, Shiozawa M, Kondo M. IV Performance Improvement of Polymer Electrolyte Fuel Cell with Porous Channel. JSAE Transactions. 2012;43:703-8.
- [5] Cho J, Ha T, Park J, Kim H-S, Min K, Lee E, et al. Analysis of transient response of a unit proton-exchange membrane fuel cell with a degraded gas diffusion layer. international journal of hydrogen energy. 2011;36:6090-8.
- [6] Cho J, Oh H, Park J, Min K, Lee E, Jyoung J-Y. Study on the performance of a proton exchange membrane fuel cell related to the structure design of a gas diffusion layer substrate. international journal of hydrogen energy. 2014;39:495-504.
- [7] Park J, Oh H, Ha T, Lee YI, Min K. A review of the gas diffusion layer in proton exchange membrane fuel cells: durability and degradation. Applied Energy. 2015;155:866-80.
- [8] Cho J, Oh H, Park J, Min K, Lee E, Jyoung J-Y. Effect of the micro porous layer design on the dynamic performance of a proton exchange membrane fuel cell. International Journal of Hydrogen Energy. 2014;39:459-68.
- [9] Tawfik H, Hung Y, Mahajan D. Metal bipolar plates for PEM fuel cell—a review. Journal of Power Sources. 2007;163:755-67.
- [10] Debe MK. Electrocatalyst approaches and challenges for automotive fuel cells. Nature. 2012;486:43-51.
- [11] Leonard ND, Artyushkova K, Halevi B, Serov A, Atanassov P, Barton SC. Modeling of low-temperature fuel cell electrodes using non-precious metal catalysts. Journal of The Electrochemical Society. 2015;162:F1253-F61.
- [12] O'Hayre R, Cha SW, Colella W, Prinz FB. Fuel Cell Fundamentals: Wiley; 2009.
- [13] Oh H, Park J, Min K, Lee E, Jyoung J-Y. Effects of pore size gradient in the substrate of a gas diffusion layer on the performance of a proton exchange membrane fuel cell. Applied Energy. 2015;149:186-93.
- [14] Zhan Z, Xiao J, Zhang Y, Pan M, Yuan R. Gas diffusion through differently

- structured gas diffusion layers of PEM fuel cells. *International Journal of Hydrogen Energy*. 2007;32:4443-51.
- [15] Weng F-B, Hsu C-Y, Su M-C. Experimental study of micro-porous layers for PEMFC with gradient hydrophobicity under various humidity conditions. *international journal of hydrogen energy*. 2011;36:13708-14.
- [16] Kariya T, Hirono T, Funakubo H, Shudo T. Effects of the porous structures in the porous flow field type separators on fuel cell performances. *International Journal of Hydrogen Energy*. 2014;39:15072-80.
- [17] Tseng C-J, Tsai BT, Liu Z-S, Cheng T-C, Chang W-C, Lo S-K. A PEM fuel cell with metal foam as flow distributor. *Energy Conversion and Management*. 2012;62:14-21.
- [18] Kumar A, Reddy RG. Modeling of polymer electrolyte membrane fuel cell with metal foam in the flow-field of the bipolar/end plates. *Journal of power sources*. 2003;114:54-62.
- [19] Liu H, Li P, Wang K. Optimization of PEM fuel cell flow channel dimensions—Mathematic modeling analysis and experimental verification. *International Journal of Hydrogen Energy*. 2013;38:9835-46.
- [20] Tsai B-T, Tseng C-J, Liu Z-S, Wang C-H, Lee C-I, Yang C-C, et al. Effects of flow field design on the performance of a PEM fuel cell with metal foam as the flow distributor. *international journal of hydrogen energy*. 2012;37:13060-6.
- [21] Yoshida T, Kojima K. Toyota MIRAI Fuel Cell Vehicle and Progress Toward a Future Hydrogen Society. *Electrochemical Society Interface*. 2015.
- [22] Takeuchi K, Kato I, Shiozawa M, Hamada S, Goto S, Kondo M, et al. Improvement of PEFC Performance by Removing GDLs. *ECS Transactions*. 2013;50:539-48.
- [23] Beuscher U. Experimental method to determine the mass transport resistance of a polymer electrolyte fuel cell. *Journal of The Electrochemical Society*. 2006;153:A1788-A93.
- [24] Baker DR, Caulk DA, Neyerlin KC, Murphy MW. Measurement of oxygen transport resistance in PEM fuel cells by limiting current methods. *Journal of The Electrochemical Society*. 2009;156:B991-B1003.
- [25] Nonoyama N, Okazaki S, Weber AZ, Ikogi Y, Yoshida T. Analysis of oxygen-transport diffusion resistance in proton-exchange-membrane fuel cells. *Journal of The Electrochemical Society*. 2011;158:B416-B23.
- [26] Kang S. Quasi-three dimensional dynamic modeling of a proton exchange membrane fuel cell with consideration of two-phase water transport through a gas diffusion layer. *Energy*. 2015;90:1388-400.
- [27] Park J. Study on the effects of structural characteristics of gas diffusion layer

- on water management and cell performance with PEM fuel cell model. Seoul: Seoul National University; 2015.
- [28] Xing L, Liu X, Alaje T, Kumar R, Mamlouk M, Scott K. A two-phase flow and non-isothermal agglomerate model for a proton exchange membrane (PEM) fuel cell. *Energy*. 2014;73:618-34.
- [29] Mueller F, Brouwer J, Kang S, Kim H-S, Min K. Quasi-three dimensional dynamic model of a proton exchange membrane fuel cell for system and controls development. *Journal of Power Sources*. 2007;163:814-29.
- [30] Fuller EN, Schettler PD, Giddings JC. New method for prediction of binary gas-phase diffusion coefficients. *Industrial & Engineering Chemistry*. 1966;58:18-27.
- [31] Perry RH, Green DW. *Perry's Chemical Engineers' Platinum Edition*: McGraw-Hill; 1999.
- [32] Fairbanks D, Wilke C. Diffusion coefficients in multicomponent gas mixtures. *Industrial & Engineering Chemistry*. 1950;42:471-5.
- [33] Maiello ML, Hoover MD. *Radioactive Air Sampling Methods*: CRC Press; 2010.
- [34] Cunningham RE. *Diffusion in gases and porous media / R.E. Cunningham and R.J.J. Williams*. New York: Plenum Press; 1980.
- [35] Krishna R, Wesselingh J. The Maxwell-Stefan approach to mass transfer. *Chemical Engineering Science*. 1997;52:861-911.
- [36] Spiegel C. *PEM fuel cell modeling and simulation using MATLAB*: Academic press; 2011.
- [37] Mench MM. *Fuel Cell Engines*: Wiley; 2008.
- [38] Wang C, Cheng P. Multiphase flow and heat transfer in porous media. *Advances in heat transfer*. 1997;30:93-196.
- [39] Kumbur E, Sharp K, Mench M. On the effectiveness of Leverett approach for describing the water transport in fuel cell diffusion media. *Journal of Power Sources*. 2007;168:356-68.
- [40] Kaviany M. *Principles of Heat Transfer in Porous Media*: Springer New York; 2012.
- [41] Jeong N, Choi DH, Lin C-L. Prediction of Darcy–Forchheimer drag for micro-porous structures of complex geometry using the lattice Boltzmann method. *Journal of Micromechanics and Microengineering*. 2006;16:2240.
- [42] Ye X, Wang C-Y. Measurement of Water Transport Properties Through Membrane-Electrode Assemblies I. Membranes. *Journal of the Electrochemical Society*. 2007;154:B676-B82.
- [43] Marr C, Li X. Composition and performance modelling of catalyst layer in a

- proton exchange membrane fuel cell. *Journal of Power Sources*. 1999;77:17-27.
- [44] Zhang J, Tang Y, Song C, Zhang J, Wang H. PEM fuel cell open circuit voltage (OCV) in the temperature range of 23 C to 120 C. *Journal of power sources*. 2006;163:532-7.
- [45] Um S, Wang CY, Chen K. Computational fluid dynamics modeling of proton exchange membrane fuel cells. *Journal of the Electrochemical society*. 2000;147:4485-93.
- [46] Bertuccio A, Vetter G. *High Pressure Process Technology: fundamentals and applications*: Elsevier Science; 2001.
- [47] White FM. *Fluid Mechanics*: McGraw Hill; 2011.
- [48] El-kharouf A, Mason TJ, Brett DJ, Pollet BG. Ex-situ characterisation of gas diffusion layers for proton exchange membrane fuel cells. *Journal of Power Sources*. 2012;218:393-404.
- [49] Ostadi H, Rama P, Liu Y, Chen R, Zhang X, Jiang K. 3D reconstruction of a gas diffusion layer and a microporous layer. *Journal of Membrane Science*. 2010;351:69-74.
- [50] Eikerling M, Kulikovskiy A. *Polymer Electrolyte Fuel Cells: Physical Principles of Materials and Operation*: CRC Press; 2014.
- [51] Lopez-Haro M, Guétaz L, Printemps T, Morin A, Escribano S, Jouneau P-H, et al. Three-dimensional analysis of Nafion layers in fuel cell electrodes. *Nature communications*. 2014;5.
- [52] Paddison SJ, Promislow KS. *Device and Materials Modeling in PEM Fuel Cells*: Springer New York; 2008.
- [53] Song C, Tang Y, Zhang JL, Zhang J, Wang H, Shen J, et al. PEM fuel cell reaction kinetics in the temperature range of 23–120 C. *Electrochimica Acta*. 2007;52:2552-61.

초 록

고분자 전해질형연료전지(PEMFC)는 기존 내연기관을 대체할 차세대 자동차 친환경 에너지원으로 주목을 받고 있다. 하지만 이는 아직은 높은 연료전지 스택의 가격 때문에 자동차 시장에서 큰 경쟁력을 갖지 못하고 있다. 따라서 스택의 가격 절감을 위하여 각각의 단위 셀의 성능을 개선시키는 등의 많은 연구가 진행되어 왔다. 이러한 연구는 크게 두 가지로 요약될 수 있는데, 첫째는 접촉저항 및 전해질막 저항에서 유발되는 저항손실(Ohmic loss)을 낮추는 연구이며, 둘째는 셀 내부에서의 산소전달저항을 줄여, 반응기체인 산소의 전달을 향상시킴으로 활성화손실(Activation loss)과 물질전달손실(Mass transport loss)을 줄이는 연구이다. 최근 들어, 후자인 반응기체의 효과적인 전달을 개선하는 연구가 재조명 받고 있다. 산소의 전달은 연료전지 내의 산소 전달저항에 비례하게 되는데 이 산소전달저항을 구하기 위하여는 위치에 따른 정확한 산소의 농도 및 산소의 전달 속도를 필요로 하기에 직접 측정하기에는 한계가 있다. 따라서 산소확산저항을 측정하는 방법으로 컴퓨터 모델링 방법이 진행되고 있다.

이번 연구는 기존의 준 3차원 모델을 개선하여 다양한 운전영역에 따른 산소전달저항을 분석할 수 있는 도구를 만드는 것을 목적으로 한다. 따라서 산소확산 메커니즘을 분자확산, 크누센확산, 이오노머 확산으로 세부화하여 모델에 반영하였으며, 또한 구형의 축매집적체(Agglomerate) 모델을 반영하여 산소 이동 현상을 더욱 자세히 묘사하였다.

이 모델은 다른 물성을 가진 두 종류의 기체확산층(GDL)에 대한 검증을 진행하였다. 첫째, 산소 2퍼센트를 포함한 질소와 헬륨, 두 종류의 혼합가스를 사용하여 한계전류밀도 값을 측정하였고 전체 산소전달저항 및 확산저항의 비율을 검증하였다. 둘째, 대기 중의 공기를 반응 기체로 사용하여 전압-전류 곡선을 측정한 후 이를 모델에서 도출된 값과

비교하였다. 검증된 모델은 기체확산층의 물리적 특성이 연료전지 산소전달저항에 미치는 영향을 다양한 전류밀도에서 분석하였다.

본 연구를 통하여 기존의 준 3차원 모델을 다양한 작동전류밀도에서 산소전달저항을 예측할 수 있도록 개선하였다. 이와 같이 개선된 모델은 연료전지의 부품에 따른 산소전달저항의 변화를 측정함으로써 부품들의 성능을 측정하는 하나의 도구로서의 잠재적 가능성을 보여주었다.

주 요 어 : 고분자 전해질형 연료전지, 산소 전달 저항, 준 3차원 모델, 기체확산층

학 번 : 2014-21886